galaxies

MDPI

Article

Radio Properties of Narrow-Line and Broad-Line Seyfert 1 Galaxies

Krisztina É. Gabányi [1,2,3,4,*], S. Komossa [5], Attila Mezősi [1], Emese Forgács-Dajka [1,2,6] and Sándor Frey [1,2]

1 Department of Astronomy, Institute of Physics and Astronomy, ELTE Eötvös Loránd University, Pázmány Péter sétány 1/A, 1117 Budapest, Hungary; ytserrof@student.elte.hu (A.M.); forgacs.emese@ttk.elte.hu (E.F.-D.); frey.sandor@csfk.org (S.F.)
2 Konkoly Observatory, HUN-REN Research Centre for Astronomy and Earth Sciences, MTA Centre of Excellence, Konkoly-Thege Miklós út 15-17, 1121 Budapest, Hungary
3 HUN-REN–ELTE Extragalactic Astrophysics Research Group, ELTE Eötvös Loránd University, Pázmány Péter sétány 1/A, 1117 Budapest, Hungary
4 Institute of Astronomy, Faculty of Physics, Astronomy and Informatics, Nicolaus Copernicus University, Grudziądzka 5, 87-100 Toruń, Poland
5 Max-Planck-Institut für Radioastronomie, Auf dem Hügel 69, D-53121 Bonn, Germany
6 HUN-REN–SZTE Stellar Astrophysics Research Group, 766 Szegedi Rd., 6500 Baja, Hungary
* Correspondence: k.gabanyi@astro.elte.hu

Abstract

Narrow-line Seyfert 1 (NLS1) galaxies host active galactic nuclei (AGN) with narrow optical emission lines of the broad-line region. This is often explained with a relatively lower mass of the central supermassive black hole and super-Eddington accretion. We compared the radio properties of large samples of NLS1 and broad-line Seyfert 1 (BLS1) galaxies compiled from the Sloan Digital Sky Survey. We cross-matched the NLS1 and BLS1 samples with the Faint Images of the Radio Sky at Twenty-Centimeters (FIRST) sky survey at 1.4 GHz and the first and second epoch data of the Very Large Array Sky Survey (VLASS) at 3 GHz. We calculated the radio spectral indices, the 1.4-GHz radio power, and the radio loudness. We found lower 1.4-GHz radio detection rates for the NLS1 galaxies. The median radio loudness values, the fraction of radio-loud AGN, and the median 1.4-GHz radio power are also lower for the NLS1 sample. The median spectral indices imply a slightly steeper radio spectrum for the NLS1 sample than for the BLS1 sample. Comparison of the star formation rates estimated from the radio data and the infrared measurements of the Wide-field Infrared Survey Explorer satellite indicated that more than half of the FIRST- and VLASS-detected NLS1 and BLS1 galaxies contain radio-emitting AGN.

Keywords: active galactic nuclei; star formation; Seyfert 1 galaxies; radio continuum; infrared measurements

Check for updates

Academic Editor: Alexei V. Moiseev

Received: 2 June 2026
Revised: 30 July 2026
Accepted: 5 August 2026
Published: 12 August 2026

Copyright: © 2026 by the authors. Licensee MDPI, Basel, Switzerland. This article is an open access article distributed under the terms and conditions of the Creative Commons Attribution (CC BY) license.

1. Introduction

Narrow-line Seyfert 1 galaxies (NLS1) are a peculiar subgroup of active galactic nuclei (AGN) showing narrow optical emission lines from the broad-line region (BLR). The full-width at half maximum (FWHM) of the broad Hβ line is $<$2000 km s^{-1}, the flux ratio of the [O III]λ5007 to Hβ line is $<$3 [1,2]. They are often characterized by strong emission of the Fe II multiplets [3]. Such properties are explained by the high accretion rate of a relatively smaller mass supermassive black hole (see a review by, e.g., [4]).

While most NLS1 galaxies are radio-quiet, their radio properties are diverse, ranging from weak radio emitters to rare systems hosting powerful relativistic jets. NLS1s

are more radio-quiet than the general AGN population, with ∼7% of them being radio-loud [5,6]. At low radio frequencies, a recent study [6] reported detection rates as high as 40% at 144 MHz in the Low-Frequency Array (LOFAR) Two-metre Sky Survey (LoTSS, [7]) Data Release 3 (DR3). Additionally, there are a number of extremely radio-loud NLS1 galaxies showing properties similar to blazars, AGN with jets pointing close to the line of sight, such as relativistic jets, and even gamma-ray emission (e.g., Refs. [5,8–10] and references therein).

The interpretation of the radio properties of NLS1 galaxies can be complicated by selection effects and by ambiguities in the optical classification of large samples [6,11]. Therefore, a comparison with an appropriate control sample is essential when assessing whether the observed trends reflect intrinsic differences between narrow- and broad-line type 1 AGN or arise from sample selection. This is particularly important when radio loudness and related quantities are investigated, since extinction and reddening can affect the optical measurements and thereby bias their interpretation [5,12].

Recently, Ref. [12] published catalogs of NLS1 and broad-line Seyfert 1 galaxies (BLS1) based on the spectra of the Sloan Digital Sky Survey Data Release 17 (SDSS DR17, [13]). They considered objects classified as either galaxies or quasars with redshift $z < 0.8$ to make sure that both the Hβ and the [O III] emission lines fall within the spectral range of SDSS and excluded objects with low signal-to-noise ratio (SNR) or with otherwise flagged data. They updated the SDSS pipeline-based redshift values with the improved redshift measurements of the SDSS DR16 [14]. They used the publicly available Bayesian AGN Decomposition Analysis for SDSS Spectra (BADASS, [15]) code to classify these sources. Most of the objects were type 2 AGN; the remainder, nearly 75,000 objects, were classified into either NLS1 or BLS1 categories. This classification was based on the FWHM of the broad Hβ emission line and the flux ratio of the [O III] and Hβ emission lines. Thus, their final NLS1 catalog contained 22,656 objects, while the other 52,273 were classified as BLS1 galaxies.

The radio loudness of the samples was investigated by cross-matching them with the Faint Images of the Radio Sky at Twenty-Centimeters (FIRST, [16]) survey data and assuming the same spectral index for all objects [12]. Here, we extend this comparison by investigating the radio properties of the NLS1 and BLS1 samples in a uniform framework using the FIRST as well as the more recent Very Large Array Sky Survey (VLASS, [17]). Our aim is to test whether the two classes differ in their radio detection rate, spectral index, radio loudness, and 1.4-GHz radio power. We also assess to what extent the observed radio emission can be related to AGN activity rather than star formation.

Paliya et al. (2024) [12] noted that they did not discriminate their objects by optical magnitude. However, they list the absolute B-band magnitude (M_B) in their catalogs. Therefore, when comparing their data in the BLS1 and NLS1 catalogs, we divided them into quasar and Seyfert galaxy populations using the limiting value of $M_B = -23$ [18]. In the following, we will refer to the two catalogs of [12] as BL1 and NL1 containing the broad-line type 1 and the narrow-line type 1 AGN, respectively. We will differentiate between the optically brighter and fainter subsamples as type 1 quasars and Seyfert 1 galaxies, respectively. We will refer to these subsamples as narrow-line type 1 quasars or NLQ1, narrow-line Seyfert 1 galaxies or NLS1 galaxies, broad-line type 1 quasars or BLQ1, and broad-line Seyfert 1 galaxies or BLS1 galaxies.

The paper is structured as follows. In Section 2, we describe the samples, the radio cross-matching procedure, and the construction of the subsamples used in the analysis. In Section 3, we present the main radio properties of the NL1 and BL1 sources, including their detection rates, spectral indices, radio loudness, radio power, and compactness. In Section 4, we discuss the implications of these results, with particular emphasis on

the origin of the radio emission and on the role of AGN activity and star formation. In Section 5, we summarize our main conclusions. During the analysis, we identified a few individual sources with extremely large spectral indices or radio loudness. These are listed in Appendices C and D, respectively. In the following, we assume a flat ΛCDM cosmological model with $H_0 = 70\,\mathrm{km\,s^{-1}\,Mpc^{-1}}$ and $\Omega_\mathrm{m} = 0.3$. We use the radio spectral index α defined as $S \propto \nu^\alpha$, where S is the flux density, and ν is the observing frequency.

2. The Samples

In the BL1 and NL1 catalogs of [12], there are 52,273 and 22,656 objects, respectively. However, we found that there are 276 duplicate entries that refer to the same optical objects in the BL1 catalog. Thus, there are 51,997 unique objects in the BL1 catalog. Similarly, we found 63 duplicates in the NL1 catalog. Later, we found three objects among the five extremely radio-loud ones in the NL1 sample whose optical spectra could be better described with heavily-obscured AGN; therefore, we removed them from the following analysis (for more details, see Appendix D). Thus, 22,590 unique NL1 AGN remained.

Following [12], we cross-matched their catalogs with the FIRST using a search radius of 5″. We also checked within the FIRST catalog whether there are multiple detections within this search radius. We found 13 and 1 such objects in the BL1 and NL1 samples, respectively. We inspected the FIRST cutout images of the objects having multiple FIRST counterparts and found that in all but two cases (both BL1 AGN), the multiple radio emissions can most probably be connected to a single optical galaxy, the one listed in the catalog of [12]. For those objects, we included the summed flux density of the FIRST counterparts in our final catalog.

The two exceptions are SDSS J161318.18+341544.0 and SDSS J1222517.95+222018.6. The first one showed a rather diffuse radio structure in its FIRST image described by two components in the catalog. However, both of those have rather high sidelobe probability, 0.526 and 0.282; therefore, we did not include this object as a radio detection. For SDSS J1222517.95+222018.6, we retained as the FIRST counterpart the detection that has lower sidelobe probability (0.016 versus 0.027). Thus, we recovered 727 and 2567 FIRST counterparts for the NL1 and the BL1 samples, respectively.

Principally, there could be chance coincidences among these counterparts. To estimate the probability of finding unrelated radio emissions to the optical galaxies within the FIRST catalog using a search radius of 5″, we created false lists of optical coordinates by adding 1°, 2°, and 3° to the right ascension coordinates in the BL1 and NL1 catalogs and checked for FIRST detections with the same 5″ search radius. (A similar method was employed by, e.g., [19,20], when cross-matching the Quaia [21] and the VLASS and the FIRST and SDSS catalogs, respectively). Since we do not expect radio emission at these "fake" optical positions, the found FIRST objects would indicate the rate of false detections. We found false detection rates of (0.04–0.08)%; thus, at most, two mistakenly identified BL1 FIRST sources and one NL1 FIRST source are expected.

As a next step, we looked for counterparts of the FIRST-detected objects in the VLASS catalogs. We used a search radius of 1.5″ around the optical positions listed in the catalogs. We used the publicly available VLASS quick-look catalogs[1]. These are available for the first and second observing epochs of the VLASS. We used the third and the second pipeline versions of the epoch 1 and epoch 2 data, respectively (available at the time when the analysis was performed). Following the CIRADA VLASS Catalog User Guide[2], we disregarded entries with `Duplicate_flag` < 2, and `Quality_flag` not equal to 0 or 4, and we only used entries with `S_code` not equal to 'E'. These settings ensured the exclusion of sidelobe structures and other false detections that may appear in the VLASS catalogs.

For a couple of objects with multiple FIRST counterparts within the 5″ FIRST search radius, we checked all of those FIRST positions whether they have VLASS counterparts. If multiple VLASS sources were found (in 8 cases), we included their summed flux densities in the final catalog. These objects are listed in Table A1 in the Appendix. At the end, among the BL1 and the NL1 sources detected in the FIRST, we found 1883 and 434 counterparts in the first-epoch VLASS catalog and 1869 and 445 in the second-epoch VLASS catalog. These correspond to fractions of ∼73% and ∼60% for the FIRST-detected BL1 and NL1 AGN, respectively.

Due to the non-concurrent nature of the two radio surveys, source variability can influence the analysis. With performing the same analysis using two different epochs of the VLASS (separated by one to five years in time), we can qualitatively assess the robustness of the obtained results versus the unknown source variability.

We note that our radio-counterpart search method is not sensitive to the galaxies showing bright, extended radio lobes, with very faint central radio emission, below the FIRST detection limit. To investigate the extended radio emission, lower-frequency surveys, e.g., those conducted by the LOFAR such as the LoTSS, Ref. [7], can be more relevant, as illustrated by, e.g., Ref. [6], who reported LOFAR detections of NLS1 galaxies.

In the following, we refer to the FIRST+VLASS1 and FIRST+VLASS2 for our samples of BL1 and NL1 AGN detected in FIRST and during the VLASS epoch 1 or VLASS epoch 2 surveys, respectively. The data tables of the FIRST- and VLASS-detected NL1 and BL1 AGN are available at the Zenodo archive via https://doi.org/10.5281/zenodo.20451035 (accessed 2 June 2026).

3. Results

3.1. Radio Detections

We found that 6342 out of the unique 51,997 BL1, and 2707 out of the unique 22,590 NL1 AGN do not fall into the FIRST sky coverage. Taking the FIRST coverage into account, the 1.4-GHz detection rates of the objects in the NL1 and BL1 catalogs are ∼3.7% and ∼5.6%, respectively, at the detection limit of the FIRST, ∼1 mJy. According to the statistical Z-test [22], the probability that these proportions are not different is less than 0.1%.

The distributions of Seyfert 1 galaxies and type 1 quasar among the NL1 and BL1 sources that fall within the FIRST coverage are listed in Table 1. Among the FIRST-detected ones, there are 250 and 1046 NL1 and BL1 galaxies, respectively, with optical B-band magnitudes fainter than −23, thus, traditionally regarded as Seyfert galaxies. Thus, the 1.4-GHz radio detection rates of the NLS1 and BLS1 galaxies are 1.7% and 4.3%, respectively. The Z-test indicates that these 1.4-GHz radio detection rates are different at a significance level of >99%. Among the FIRST-detected AGN, there are 476 and 1515 sources brighter than −23 magnitude, thus, traditionally regarded as quasars. (There were a few objects without M_B values in the NL1 and BL1 catalogs). Thus, the 1.4-GHz detection rates of the NLQ1 and BLQ1 AGN are 10.1% and 7.2%, respectively.

Table 1. Number of NL1 and BL1 sources falling within the FIRST coverage and with 1.4-GHz radio detections in the FIRST.

Sample	Within the FIRST Coverage	FIRST Detection
NL1 all	19,883	727
NLQ1	4694	476
NLS1	15,152	250
BL1 all	45,655	2567
BLQ1	21,131	1515
BLS1	24,424	1046

3.2. Spectral Index

We calculated the two-point spectral index between 1.4 GHz and 3 GHz for the objects in the FIRST+VLASS1 and in the FIRST+VLASS2 samples. We flagged the objects with relative flux density errors exceeding 30% in either of the two radio surveys. These were only a handful of sources, 3 and 10 NL1 and BL1 AGN in the FIRST+VLASS1 sample, and 4 and 5 NL1 and BL1 AGN in the FIRST+VLASS2 sample, respectively. We excluded them from further analysis. A few spectral index values were larger than the theoretically possible one for the optically thick synchrotron emission, 2.5. We excluded those 2 and 8 objects from the NL1 and BL1 samples, respectively, from the following distribution comparison. (Their details are given in Appendices C.1 and C.2). Finally, we grouped the sources according to their M_B into optically bright (quasar) and fainter (Seyfert galaxy) categories. There were 1 and 7 (5 in the FIRST+VLASS2) objects in the NL1 and BL1 catalogs, respectively, lacking M_B values; thus, they could not be assigned to either of the two groups.

The histograms of the spectral index distributions for the FIRST+VLASS1 and FIRST+VLASS2 are shown in Figure 1. The median spectral indices, the first (Q_1) and third quartiles (Q_3), and interquartile ranges (IQR) of the distributions are listed in Table 2. Box diagram representations of the distributions and quartile values are shown in Figure 2. The differences between the spectral indices obtained using the two epochs of the VLASS arise from source variability and possible differences between the data reduction pipelines. As illustrated by the plots and the qualitative details of the distributions, there are no major differences whether the first or the second epoch of VLASS data were used. Thus, flux density variability of individual sources, and the different conditions of the VLASS observing epochs do not influence our results at a statistical level.

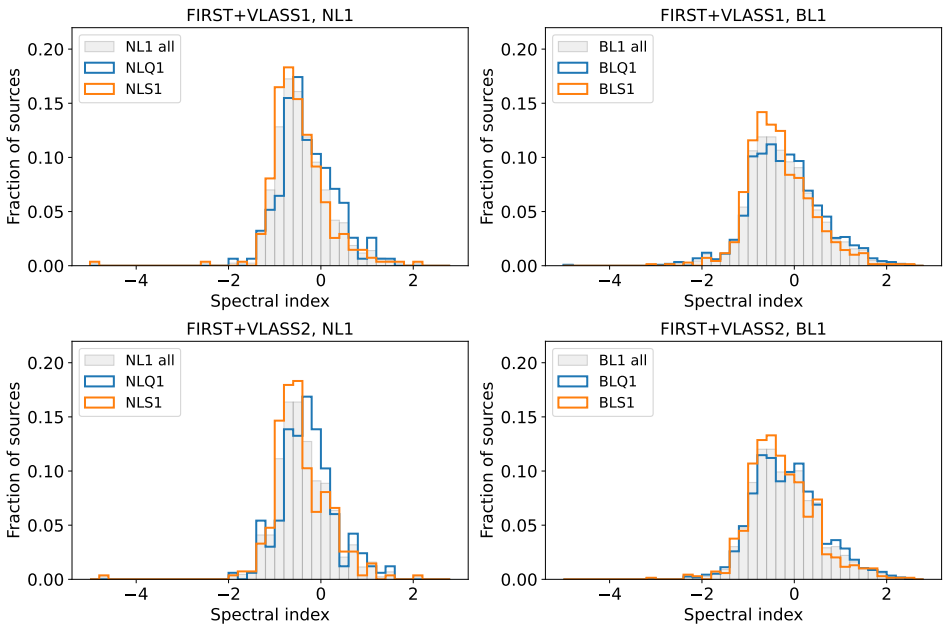

Figure 1. Distributions of the radio spectral index values of the NL1 and BL1 samples of [12]. In all panels, blue and yellow colors are for the respective type 1 quasar and Seyfert 1 galaxy subgroups. Grey filled histograms show the whole samples. The top row is for the FIRST+VLASS1; the bottom row is for the FIRST+VLASS2 samples.

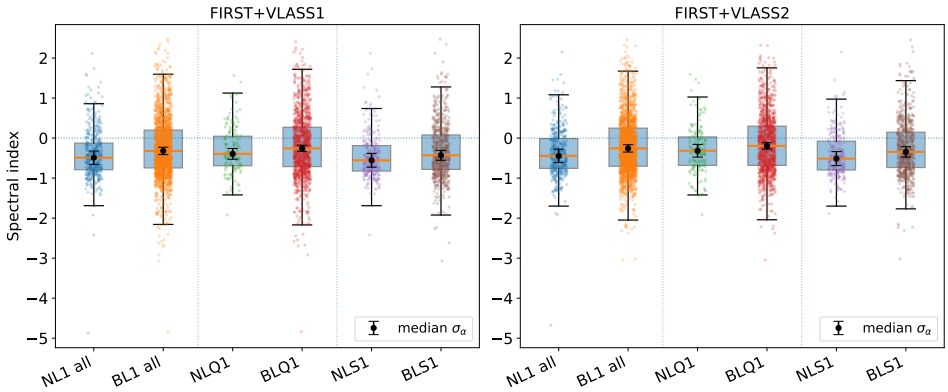

Figure 2. Boxplot representation of the spectral index distributions of the NL1 and BL1 AGN for the FIRST+VLASS1 (**left panel**) and FIRST+VLASS2 (**right panel**) samples. The boxes extend from the first quartile, Q_1, to the third quartile, Q_3, and therefore, enclose the central 50% of the data. The horizontal line inside each box marks the median spectral index. The whiskers extend to the most extreme data points within 1.5 times of the interquartile range, and the faint points show the individual sources. The black points and error bars indicate the median spectral index and the median of the individual spectral index uncertainties, σ_α, for the corresponding subsample. These error bars represent the typical uncertainty of individual spectral index measurements, not the uncertainty of the median. The dotted horizontal lines show the $\alpha = 0$ value to guide the eye only. The vertical dotted lines separate group pairs.

Table 2. Spectral index statistics of the NL1 and BL1 samples. The table lists the number of sources, the median spectral index, the first and third quartiles (Q_1, Q_3), the interquartile range (IQR), and the median of the individual spectral index uncertainties (σ_α) in cols. 3, 4, 5, 6, 7, and 8, respectively.

Data Set	Subsample	No.	Median α	Q_1 (α)	Q_3 (α)	IQR (α)	Median σ_α
FIRST+VLASS1	NL1 all	429	−0.49	−0.79	−0.13	0.67	0.17
	BL1 all	1867	−0.32	−0.74	0.20	0.94	0.09
	NLQ1	155	−0.39	−0.69	0.05	0.74	0.14
	BLQ1	1169	−0.26	−0.71	0.27	0.98	0.08
	NLS1	273	−0.56	−0.82	−0.19	0.64	0.17
	BLS1	691	−0.43	−0.78	0.08	0.86	0.12
FIRST+VLASS2	NL1 all	440	−0.45	−0.76	−0.01	0.74	0.17
	BL1 all	1857	−0.26	−0.70	0.25	0.95	0.09
	NLQ1	166	−0.32	−0.68	0.03	0.71	0.16
	BLQ1	1160	−0.20	−0.68	0.30	0.98	0.08
	NLS1	273	−0.51	−0.80	−0.08	0.72	0.18
	BLS1	692	−0.35	−0.74	0.15	0.88	0.13

All of the median spectral index values are $\alpha > -0.6$, formally indicating flat radio spectra. This is expected since we selected objects detected both in the FIRST and in the VLASS with mostly compact morphology; therefore, we expect a generally flat spectrum. The median value for the BLQ1 subsample corresponds to the flattest radio spectrum, and the median value obtained for the NLS1 subsample corresponds to the steepest radio spectrum.

In Table 2, we report the median of the spectral index errors of the different samples. The median individual uncertainty is smaller than the interquartile range of the corresponding spectral index distribution. Therefore, the observed spread of the spectral index values is not dominated by the measurement uncertainties.

To further test whether the observed median spectral index differences between the NL1 and BL1 samples are robust against the propagated measurement uncertainties, we performed a Monte Carlo perturbation test. In each realization, every spectral index was perturbed according to its individual uncertainty, $\alpha_{\rm MC} \sim \mathcal{N}(\alpha, \sigma_\alpha)$, and the difference in

the median spectral indices, $\Delta\alpha_{\rm MC}$, was computed. We considered three comparisons: the full NL1–BL1 samples, the type 1 quasar subsamples, NLQ1–BLQ1, and the Seyfert 1 subsamples, NLS1–BLS1. (The tests were performed for both the FIRST+VLASS1 and FIRST+VLASS2). For all three comparisons, $\Delta\alpha_{\rm MC}$ was defined as the median spectral index of the NL1-like group minus that of the corresponding BL1-like group. Thus, negative values indicate that the NL1 group has a steeper median spectral index. The Monte Carlo distributions remained centered close to the observed median spectral-index differences, $\Delta\alpha_{\rm obs}$, and their central 16–84 percentile intervals do not include zero (Figure 3). This shows that the observed NL1/BL1 spectral-index differences are robust against the propagated flux-density measurement uncertainties.

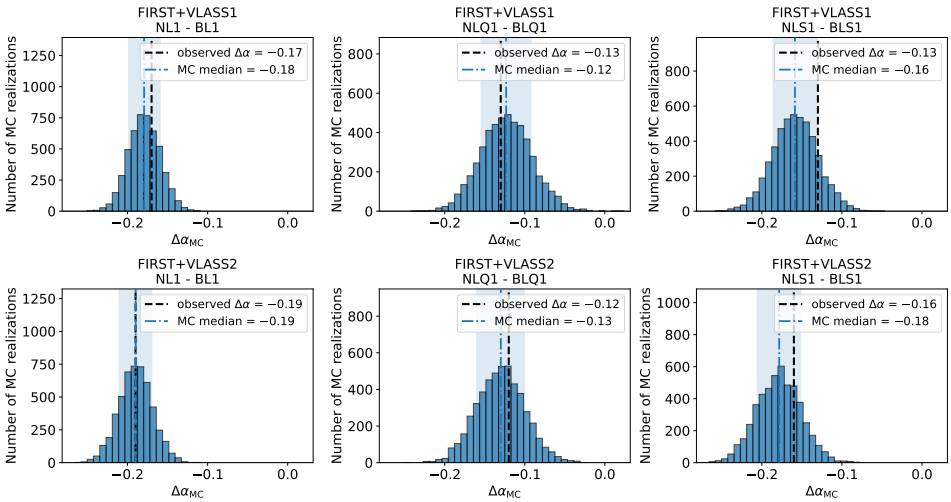

Figure 3. Monte Carlo perturbation test of the median spectral index differences between the NL1 and BL1 samples. In each realization, every spectral index was perturbed according to its individual uncertainty, and the median difference $\Delta\alpha_{\rm MC} = {\rm median}(\alpha_{\rm NL1-like}) - {\rm median}(\alpha_{\rm BL1-like})$ was recomputed. The panels show the resulting $\Delta\alpha_{\rm MC}$ distributions for the full samples, the QSO subsamples, and the Seyfert subsamples, separately for the FIRST+VLASS1 and FIRST+VLASS2 datasets. The shaded blue regions show the 16th–84th percentile interval of the $\Delta\alpha_{\rm MC}$ distributions. The black dashed line marks the observed median difference of the spectral indices, while the blue dash-dotted line marks the median of the Monte Carlo distribution. Negative values mean that the NL1 group has a steeper median spectral index than the corresponding BL1 group. The Monte Carlo distributions remain separated from zero, indicating that the observed NL1/BL1 differences are robust against the propagated measurement uncertainties.

The redshift distributions of the objects retained for the radio spectral index calculation are shown in Figure 4. It is clear that the optically fainter Seyfert galaxy subgroups are not well sampled at high redshifts, where the brighter, quasar objects dominate. To test whether this can influence our results of the spectral index differences, we examined whether the redshift distributions of the NL1 and BL1 populations are statistically compatible. The comparisons were performed separately for the full samples, the type 1 quasar-like subsamples, and the Seyfert 1-like subsamples, and we used two complementary methods.

First, we compared whether using different redshift cuts on the data can provide samples with statistically compatible redshift distributions. For each tested redshift cut, we compared the redshift distributions of the the NL1–BL1, NLQ1–BLQ1, and NLS1–BLS1 samples (for the two VLASS epochs) via the Kolmogorov–Smirnov, e.g., [23] and the Anderson–Darling, AD, [24] statistical tests. If both tests failed to reject at a significance level of 5%, the null hypothesis that the two samples are drawn from the same redshift distribution, we regarded the redshift distributions of those two samples as compatible, not showing significant differences.

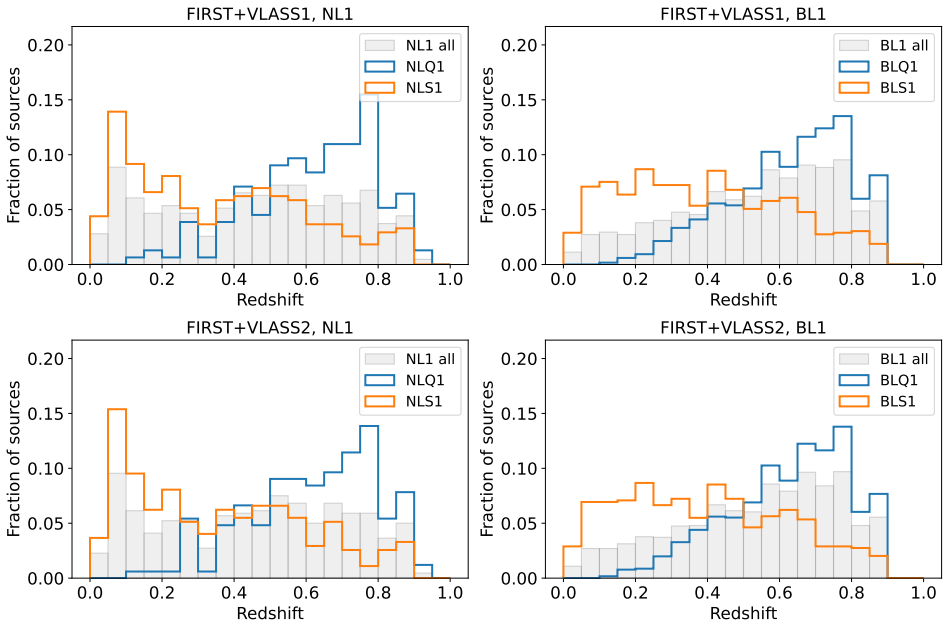

Figure 4. Redshift distributions of the the FIRST- and VLASS-detected NL1 and BL1 samples of [12] retained for the spectral index calculation. The details of the plots are the same as in Figure 1.

We found that by restricting the samples for AGN with $z > 0.3$, the redshift distributions of the pairwise compared samples no longer displayed significant differences. Then, we compared the radio spectral index distributions of the NL1-like and corresponding BL1-like groups in both the full and the $z > 0.3$ samples. The comparisons were performed separately for the NL1–BL1, NLQ1–BLQ1, and NLS1–BLS1 sample pairs and for both VLASS epochs, using the two-sample KS and AD statistical tests. The results are presented in detail in Appendix B and in Table A3. The full and $z > 0.3$ samples give the same qualitative results.

As a second test, we applied a redshift-matched Monte Carlo resampling. Within each redshift bin, we randomly selected the same number of AGN from each of the two compared groups and recalculated the differences of the median spectral indices in each realization. While the first method applies an empirical redshift cut, the second one directly matches the redshift distributions, allowing us to test whether the observed NL1–BL1 spectral index differences remain after controlling for differences in the redshift distributions. Moreover, the redshift cut removes the entire low-redshift part of the samples, and the absence of a statistically significant difference does not imply that the remaining redshift distributions are exactly matched. The detailed description of the Monte Carlo resampling and its results are given in Appendix B. The differences between the subsamples remained even after the redshift resampling.

To summarize, we found that the observed NL1/BL1 spectral index differences remain even after controlling the redshift distributions. Applying the $z > 0.3$ cut does not change our main conclusions: the differences remain significant for the full NL1–BL1 samples and for the NLS1–BLS1 subsamples. In the case of the NLQ1–BLQ1 comparisons, the evidence for a difference is weaker for the FIRST+VLASS1 data set, when the two statistical tests gave contradictory results. However, the spectral index difference between the subgroups NLQ1 and BLQ1 is significant when using the FIRST+VLASS2 (Table A3).

3.3. Radio Loudness

The radio loudness parameter (RL) of an AGN is defined as the ratio of the 5-GHz radio flux density to the 4400 Å optical flux density [25]. Paliya et al. (2024) [12] estimated the radio loudness values from the 1.4-GHz FIRST measurement, assuming a radio spectral

index of $\alpha = -0.5$ uniformly for all sources. Since we found a broad range of actual radio spectral index values and indications of different distributions for the different groups, we recalculated the radio loudness by using the FIRST–VLASS spectral indices, to estimate the expected 5-GHz flux densities of each source individually.

To obtain the 4400 Å optical flux density, we calculated the B-band magnitudes from the SDSS-measured g and r magnitudes using the same formula as in [12]. We used the SDSS DR16 [26] catalog and selected only those sources where the photometry was reliable (i.e., the 'clean photometry' flag was given as 1). The obtained magnitudes were corrected for galactic extinction using the extinction calculator provided by the NASA/IPAC Extragalactic Database[3], then the magnitudes were converted to flux densities assuming a zero-point flux density of 4260 Jy [27]. We assumed an optical spectral index of -0.5.

Similarly as was carried out for the radio spectral index investigation, we excluded those objects that have unrealistically high radio spectral indices, $\alpha > 2.5$, or have flux density measurements with relative errors $> 30\%$ in either of the two radio surveys. Additionally, we wanted to minimize the effect of dust obscuration in the host galaxy, which can artificially increase the RL value. To that end, we used the flux ratio of the Hα to Hβ emission lines. A flux ratio value of $\gtrsim$3 implies obscuration, while values above 5 indicate significant obscuring effect [28,29]. The wavelength range covered by SDSS does not allow the detection of Hα line at $z \gtrsim 0.5$ and can hinder the recognition of the line even at slightly lower redshifts as well. Therefore, we do not have information on the obscuration state of the galaxies located at $z \gtrsim 0.5$. For the RL-distribution investigation, we considered the objects that have Hα line measurements; thus, the highest-redshift ones are not used. Among the retained objects, we only used those that have Hα and Hβ flux density ratios not exceeding the value of 5.

The distributions of radio loudness values are shown in histogram and boxplot representations in Figures 5 and 6, respectively. The RL distributions of the NLQ1 are different depending on which epoch of the VLASS data is used. This can be most prominently seen in the lowest radio loudness bins in Figure 5. It is mainly due to the small sample sizes; there are only 28 and 36 NLQ1 in FIRST+VLASS1 and FIRST+VLASS2, respectively. Additionally, most of the NLQ1 that are detected only in the second VLASS epoch fall into that RL bin, with an RL value of $\sim$3.2.

Using the KS and AD statistical tests, we compared the distributions. We obtained the same results whether we used the FIRST+VLASS1 or FIRST+VLASS2 samples. The radio loudness of NL1 and BL1 samples cannot be described with the same distribution at a significance level of 95%. Additionally, the radio loudness of NLS1 galaxies and the BLS1 galaxies come from different distributions, and this is also true at the same significance levels, when comparing the NLQ1 and the BLQ1 samples. However, within the narrow-line and broad-line samples, there are no differences in the radio loudness distributions of the optically brighter (type 1 quasar) and optically fainter (Seyfert 1 galaxy) subgroups. The probability that BLQ1 and BLS1 come from different distributions is $\lesssim$5%, and similarly for the NLQ1 and NLS1 samples.

We calculated the median radio loudness values for the samples and also the median values for the objects traditionally treated as radio-loud ones, i.e., RL > 10. The resulting values are listed in Tables 3 and 4. There is no substantial difference whether the RL values are calculated using the first- or the second-epoch VLASS data. The exceptions are the median RL values of the NLQ1 subsample, showing the largest difference between the median values. This is due to the very small sample size, the low number of NLQ1 retained for radio loudness calculations. Generally, the median RL values are larger for BL1 than NL1 AGN. But if the radio-loud objects are considered only, the median RL values do not differ significantly.

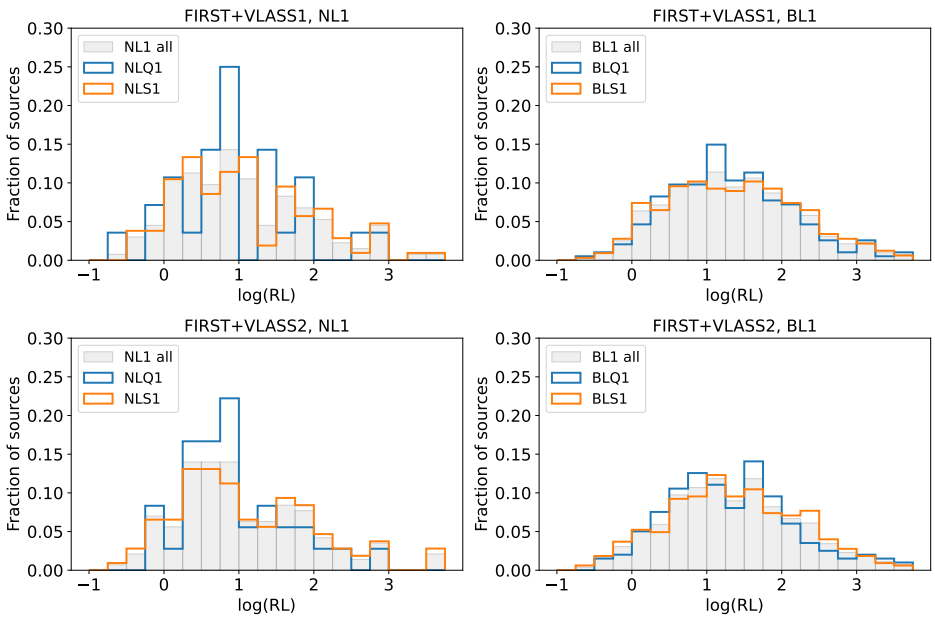

Figure 5. Distributions of the logarithm of the RL values of the NL1 and BL1 samples. The details of the figure are the same as in Figure 1.

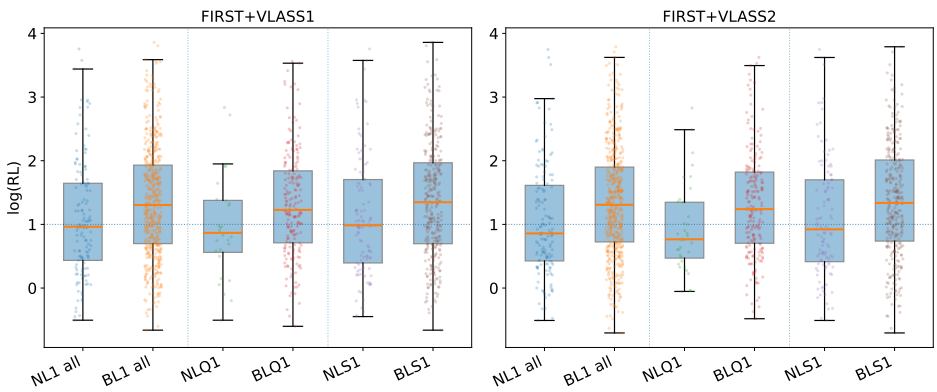

Figure 6. Boxplot representation of the radio loudness distributions of the NL1 and BL1 AGN for the FIRST+VLASS1 (**left panel**) and FIRST+VLASS2 (**right panel**) samples. The boxes extend from the first quartile, Q_1, to the third quartile, Q_3, and therefore, enclose the central 50% of the data. The horizontal line inside each box marks the median of the logarithmic radio loudness values. The whiskers extend to the most extreme data points within 1.5 times of the interquartile range, and the faint points show the individual sources. The horizontal dotted line indicates the traditional division between radio-loud and radio-quiet sources [25]. The vertical dotted lines separate group pairs.

Contrary to expectations that Seyfert galaxies are mostly radio-quiet (e.g., Ref. [30] and references therein), we found that the type 1 quasar subgroups are not more radio-loud than the Seyfert 1 galaxies in our samples. We investigated whether the intermediate sources, located just at or around the traditional quasar/Seyfert galaxy division at $M_B = -23$ mag, influence the median values. So we removed objects from the samples with $-23.5\,\text{mag} < M_B < -22.5\,\text{mag}$. This, however, did not change significantly the median RL values, except for the radio-loud NLQ1. For them, the median RL became significantly larger, 81.2 and 85.2 for the FIRST+VLASS1 and FIRST+VLASS2 samples, respectively. However, such a cut further decreased the sample sizes to only 5 sources, making the results less constrained.

We also calculated the median radio loudness values for the datasets binned according to their absolute optical magnitudes. Since the sample sizes are small, we were able to

create bins each containing ∼37 galaxies. This way, we had 4 and 14 bins for the NL1 and BL1 groups, respectively. For the radio-loud objects, RL > 10, to retain at least 4 bins for the smaller NL1 sample, each bin contained ∼16 AGN. This way, we had 4 and 20 bins for the NL1 and BL1 groups, respectively. We found no obvious trends in RL with the *B*-band optical magnitude.

Table 3. Radio loudness statistics of the NL1 and BL1 samples. The table lists the number of sources, the median radio loudness, the first and third quartiles of the radio loudness distribution, and the interquartile range calculated in logarithmic space.

Data Set	Subsample	No.	Median RL	Q_1 (RL)	Q_3 (RL)	IQR ($\log_{10}$(RL)) [dex]
FIRST+VLASS1	NL1 all	133	9.2	2.7	44.2	1.2
	BL1 all	518	20.1	5.0	85.2	1.2
	NLQ1	28	7.4	3.6	23.8	0.8
	BLQ1	194	16.9	5.1	69.3	1.1
	NLS1	105	9.7	2.5	50.6	1.3
	BLS1	324	22.3	5.0	92.8	1.3
FIRST+VLASS2	NL1 all	143	7.2	2.7	41.0	1.2
	BL1 all	524	20.3	5.3	79.3	1.2
	NLQ1	36	5.8	3.0	22.3	0.9
	BLQ1	199	17.4	5.1	66.2	1.1
	NLS1	107	8.4	2.6	50.1	1.3
	BLS1	325	21.7	5.5	102.6	1.3

Table 4. Radio loudness statistics of the traditionally radio-loud (RL > 10) AGN in the NL1 and BL1 samples. The table lists the number of sources, the median radio loudness, the first and third quartiles of the radio loudness distribution, and the interquartile range calculated in logarithmic space.

Data Set	Subsample	No.	Median RL	Q_1 (RL)	Q_3 (RL)	IQR ($\log_{10}$(RL)) [dex]
FIRST+VLASS1	NL1 all	61	51.0	20.8	152.1	0.9
	BL1 all	326	56.3	23.7	171.7	0.9
	NLQ1	10	59.9	23.8	87.2	0.6
	BLQ1	124	50.0	19.7	143.1	0.9
	NLS1	51	51.0	16.7	162.0	1.0
	BLS1	202	61.8	27.6	237.1	0.9
FIRST+VLASS2	NL1 all	61	56.4	24.6	145.8	0.8
	BL1 all	332	53.9	24.4	172.6	0.8
	NLQ1	12	45.2	22.5	95.2	0.6
	BLQ1	121	50.0	25.8	129.0	0.7
	NLS1	49	60.2	24.6	152.5	0.8
	BLS1	211	56.6	23.2	209.5	1.0

So far, we restricted the investigations to galaxies having information on their obscuration state. However, we also examined the few extremely radio-loud (log (RL) > 4) NL1 and BL1 AGN, regardless of whether they have Hα measurements available. We found that the optical spectra of three extremely radio-loud NL1 AGN are more similar to those of heavily obscured AGN. Therefore, they were removed from the NL1 sample. There are no Hα measurements for the other two extremely radio-loud NL1 and BL1 AGN, since all of them are located at $z > 0.5$. Therefore, they were not included in the RL distribution investigation. The details of the extremely radio-loud objects are given in Appendix D.

3.4. Radio Power

We calculated the K-corrected 1.4-GHz radio power, $P_{1.4\,\mathrm{GHz}}$, of the NL1 and BL1 galaxies using their FIRST flux densities, S_{FIRST}, and the FIRST–VLASS spectral indices, α, as

$$P_{1.4\,\mathrm{GHz}} = 4\pi D_{\mathrm{L}}^2 S_{\mathrm{FIRST}} (1+z)^{-\alpha-1}, \quad (1)$$

where D_{L} is the luminosity distance. We disregarded the few objects with spectral indices > 2.5 and with unreliable flux density measurements, as before. The distributions of $P_{1.4\,\mathrm{GHz}}$ are shown in Figures 7 and 8 for the whole samples and for the galaxies located at higher redshifts, with $z > 0.3$, respectively. This limiting redshift value was selected because the fainter Seyfert 1 galaxies are overrepresented at $z < 0.3$ (see Figure 4, and Section 3.2).

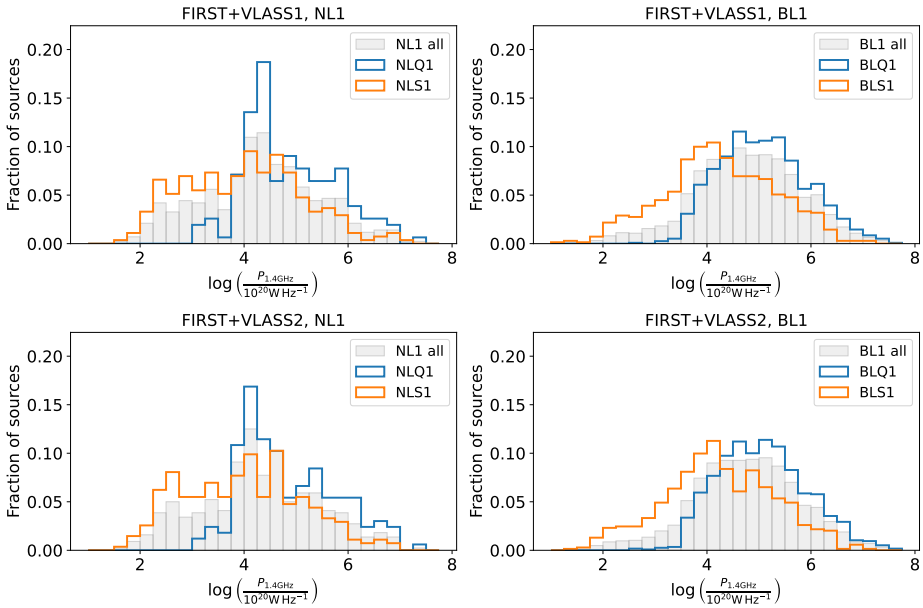

Figure 7. Distributions of the logarithm of the 1.4-GHz radio power values in units of 10^{20} W Hz^{-1} of the NL1 and BL1 samples. The details of the figure are the same as in Figure 1.

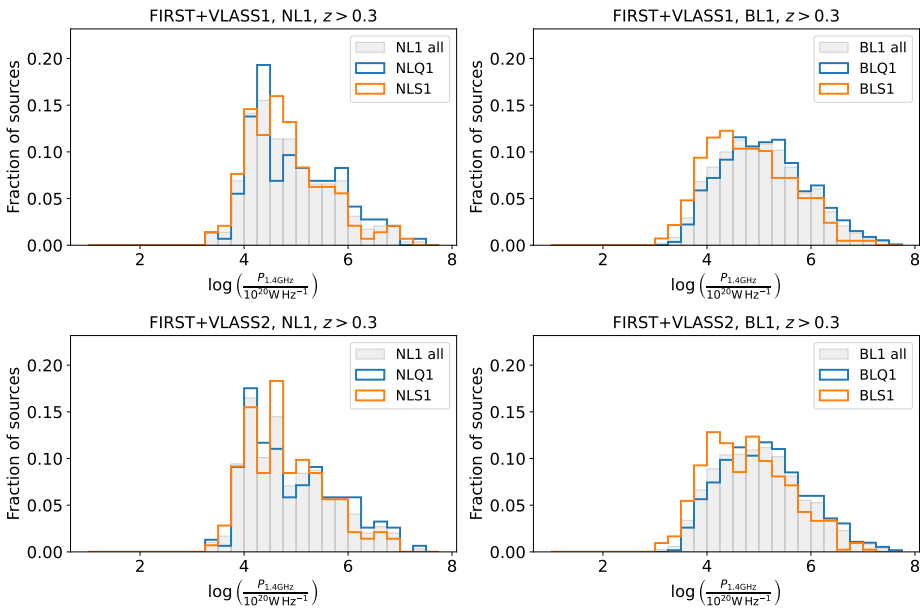

Figure 8. Distributions of the logarithm of the 1.4-GHz radio power values in units of 10^{20} W Hz^{-1} of the NL1 and BL1 samples for sources at $z > 0.3$. The details of the figure are the same as in Figure 1.

We calculated the median radio powers quartiles and interquartile ranges for the samples, for all objects (Table 5 and Figure 9), and for only those located at $z > 0.3$ (Table 6). The slight differences between the values obtained from the two epochs of VLASS data are most probably due to source variability. These differences indicate the reliability of our $P_{1.4\,\mathrm{GHz}}$ calculations. Applying the redshift cut significantly increases the median $P_{1.4\,\mathrm{GHz}}$ values for the Seyfert 1 galaxies, since this cut excludes the fainter, close-by NLS1 and BLS1 galaxies (see Figures 7 and 8).

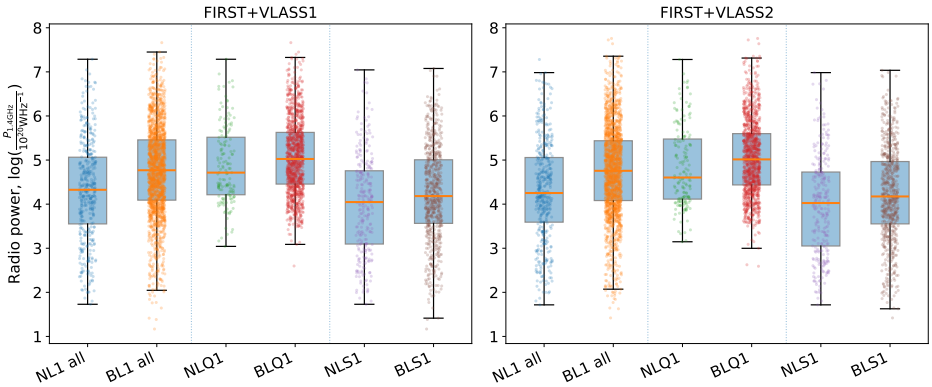

Figure 9. Boxplot representation of the FIRST radio power distributions of the NL1 and BL1 AGN. The plot details are the same as in Figure 6.

In all cases, type 1 quasars have higher median radio powers than Seyfert 1 galaxies. If restricted to $z > 0.3$ and using the second-epoch VLASS data, there is no difference between the median $P_{1.4\,\mathrm{GHz}}$ values of type 1 quasars and Seyfert 1 galaxies within the narrow-line sample, and the difference is also quite small if the first-epoch VLASS data are considered. The median $P_{1.4\,\mathrm{GHz}}$ values are similar for broad-line and narrow-line Seyfert 1 galaxies within the same redshift ranges. As a whole, the NL1 galaxies have lower median $P_{1.4\,\mathrm{GHz}}$ values than the BL1 galaxies.

To see if there is any trend in the $P_{1.4\,\mathrm{GHz}}$ values with optical absolute magnitude, we calculated the medians for different bins of M_B (Figure 10). Each bin contained 80 AGN for the BL1 and NL1 samples. The decreasing trends in the radio power with decreasing optical luminosity can be seen for both the broad- and narrow-line samples. (Although the sampling at fainter optical magnitudes is much sparser for the NL1 AGN).

Table 5. Logarithmic radio-power statistics of the NL1 and BL1 samples. The table lists the number of sources, the median, the first and third quartiles, and the interquartile range for the logarithm of the normalized radio power, $P_{20} = \frac{P_{1.4\,\mathrm{GHz}}}{10^{20}\,\mathrm{W\,Hz^{-1}}}$. The values are given for the FIRST+VLASS1 and FIRST+VLASS2 data sets above and below the horizontal line, respectively.

Subsample	No.	Median $\log_{10}(P_{20})$	Q_1 [$\log_{10}(P_{20})$]	Q_3 [$\log_{10}(P_{20})$]	IQR [$\log_{10}(P_{20})$] [dex]
NL1 all	429	4.3	3.55	5.06	1.51
BL1 all	1867	4.8	4.09	5.46	1.37
NLQ1	155	4.7	4.21	5.52	1.30
BLQ1	1169	5.0	4.46	5.63	1.17
NLS1	273	4.1	3.10	4.76	1.66
BLS1	691	4.2	3.56	5.01	1.44
ine NL1 all	440	4.3	3.59	5.06	1.47
BL1 all	1857	4.8	4.08	5.44	1.36
NLQ1	166	4.6	4.11	5.48	1.36
BLQ1	1160	5.0	4.44	5.60	1.16
NLS1	273	4.0	3.05	4.73	1.68
BLS1	692	4.2	3.55	4.97	1.41

Table 6. Logarithmic radio-power statistics of the $z > 0.3$ NL1 and BL1 AGN. The details of the table are the same as in Table 5.

Subsample	No.	Median $\log_{10}(P_{20})$	Q_1 [$\log_{10}(P_{20})$]	Q_3 [$\log_{10}(P_{20})$]	IQR [$\log_{10}(P_{20})$] [dex]
NL1 all	290	4.7	4.28	5.42	1.15
BL1 all	1543	5.0	4.40	5.58	1.18
NLQ1	145	4.8	4.33	5.55	1.22
BLQ1	1124	5.1	4.50	5.65	1.15
NLS1	144	4.7	4.20	5.26	1.06
BLS1	416	4.7	4.15	5.33	1.18
ine NL1 all	297	4.7	4.18	5.39	1.21
BL1 all	1540	5.0	4.38	5.57	1.19
NLQ1	154	4.7	4.16	5.53	1.36
BLQ1	1116	5.1	4.49	5.62	1.13
NLS1	142	4.7	4.21	5.29	1.08
BLS1	421	4.8	4.16	5.32	1.17

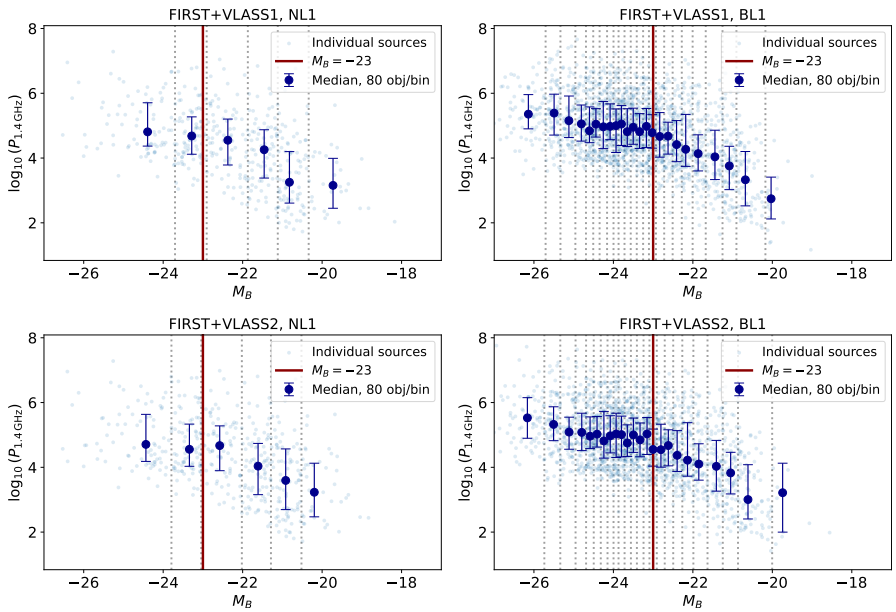

Figure 10. Optical absolute magnitude versus the logarithm of $P_{1.4\,\mathrm{GHz}}$ for the NL (**left**) and BL (**right**) samples of the FIRST+VLASS1 (**top**) and FIRST+VLASS2 (**bottom**) data. Faint points represent individual sources. Dark-blue points show the median $\log_{10}(P_{1.4\,\mathrm{GHz}})$ values in equal-number bins along the M_B axis, with 80 objects per bin. The vertical error bars show the 25–75 percentile range within each bin. Grey dotted vertical lines mark the variable-width bin boundaries, and the red vertical line marks the QSO/Seyfert division at $M_B = -23$.

Using the KS and AD statistical tests, we compared the distribution of $P_{1.4\,\mathrm{GHz}}$ values of the different subgroups. When all objects, irrespective of their redshifts, were used, the distributions of all groups were different from each other. However, when only the $z > 0.3$ objects were considered, comparing the NLS1 and BLS1 galaxies, the tests showed they came from the same distribution at a confidence level of 95%. As a whole, the 1.4-GHz radio power distributions are different from the BL1 and NL1 samples, but this is due to the different distributions of the optically brighter, type 1 quasar subgroups.

We calculated the star-formation rate, SFR, from $P_{1.4\,\mathrm{GHz}}$, assuming that all the radio flux density detected by FIRST originate from star formation, following the relation given by [31]

$$\mathrm{SFR_{FIRST}} = \frac{P_{1.4\,\mathrm{GHz}}}{1.81 \cdot 10^{21}} \times \begin{cases} 1, & \text{if } P_{1.4\,\mathrm{GHz}} > 6.4 \cdot 10^{21} \\ \left(0.1 + 0.9\left(\frac{P_{1.4\,\mathrm{GHz}}}{6.4 \cdot 10^{21}}\right)^{0.3}\right)^{-1}, & \text{otherwise} \end{cases} \quad (2)$$

where $P_{1.4\,\mathrm{GHz}}$ is in W Hz^{-1}, and SFR is obtained in M$_\odot$ yr^{-1}. The median SFRs for both samples are $\sim 10^3$ M$_\odot$ yr^{-1}, irrespective of whether the data of the first or second VLASS epochs are used. Thus, to explain the 1.4-GHz radio power, SFR values exceeding 1000 M$_\odot$ yr^{-1} would be required for half of the sources in both samples. These values are unrealistically high and indicate that jetted AGN have to contribute to the radio emission in a large fraction of sources in these samples.

3.5. Radio Compactness

To investigate the compactness of the radio emission, C_{FIRST}, we calculated the peak intensity to total flux density ratios based on the FIRST data. This ratio should fall between 0 and 1 beam^{-1}, the latter representing point-like, unresolved emission within the given survey. However, in reality, ratios often exceed 1, due to various survey-related effects, e.g., source structure not adequately described by an elliptical Gaussian brightness distribution function [16].

When calculating C_{FIRST}, we took into account the errors of the flux density, and we used 3 times the rms value as an error for the peak intensity. If $C_{\mathrm{FIRST}} > 1$ beam^{-1}, but its error allowed it to be equal to 1, we set its value to 1. Otherwise, we did not use that object for the following compactness analysis. We also excluded the objects with multiple FIRST detections, and similarly to before, objects with spectral index exceeding 2.5 and those having excessive flux density errors. The obtained distributions are shown in Figure 11. Most of the galaxies in both samples have very compact radio emission in FIRST. The median compactness values are >0.95 for all samples. Only ∼11% of NL1 and ∼20% of BL1 galaxies have compactness values below 0.8. This is not surprising, since the samples contain sources detected both in FIRST and in the higher-resolution VLASS survey, thus, they are expected to contain compact radio-emitting features.

The KS and AD statistical tests showed that the compactness distributions are different from the BL1 and NL1 samples. When comparing the optically brighter quasar subgroups of the broad- and narrow-lines samples, the tests showed different distributions, as well as when the distributions of the optically fainter NLS1 and BLS1 subgroups are compared.

We investigated the source compactness using the second-epoch VLASS data as well, C_{VLASS}. (We decided not to use the first-epoch VLASS data, since the peak intensities could be significantly underestimated at different levels at different observing times within this epoch, according to [17]). We followed the same approach as for the FIRST data: we disregarded sources if their compactness values, when taking into account the errors of the integrated flux density and peak intensity, were still exceeding unity, $C_{\mathrm{VLASS}} > 1$ beam^{-1}. We found that the median VLASS compactness is slightly lower ≈ 0.9 for both the BL1 and NL1 samples than that of C_{FIRST} and slightly larger fractions, ∼30% of the NL and ∼25% of the BL sources have $C_{\mathrm{VLASS}} \lesssim 0.8$ beam^{-1}. This shows that some sources point-like in FIRST have a slightly more resolved structure in the high-resolution VLASS observations; however, the majority of the objects remained unresolved.

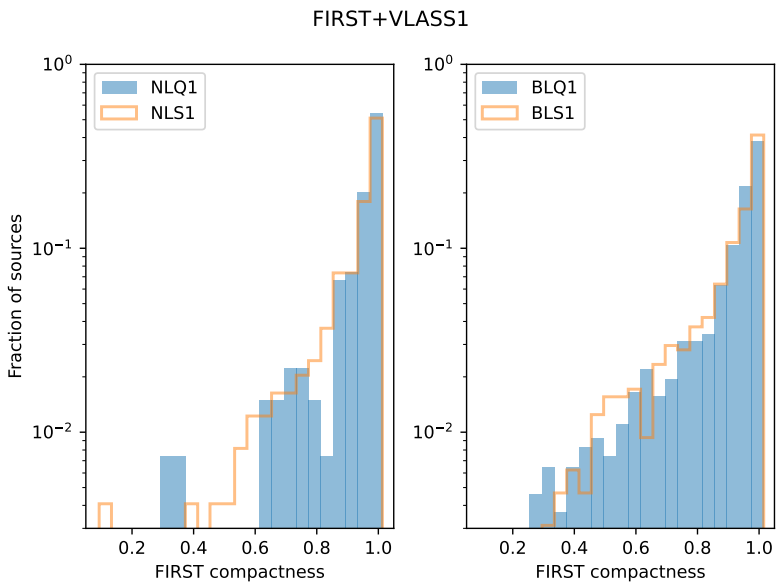

Figure 11. Distribution of FIRST compactness values for the NL1 (**left**) and BL1 (**right**) samples detected in the FIRST and in the first epoch of VLASS. Filled blue histograms represent the optically brighter type 1 quasars, orange lines the optically fainter Seyfert 1 galaxies.

4. Discussion

4.1. Origin of the Radio Emission

The FIRST detection rate is larger for the BL1 sources (∼5.6%) than for the NL1 sources (∼3.7%), and a similar difference is obtained comparing the radio detection rate of BLS1 to NLS1 galaxies. Recently, Ref. [6] investigated the radio properties of ∼4000 NLS1 galaxies based on the sample of [32], which largely overlaps with the sample of [12]. Varglund et al. (2025) [6] found a higher FIRST detection rate, ∼7.6%, for their NLS1 sample, using also 5″ positional matching radius. Arsenov et al. (2025) [19] investigated the radio-detection statistics of quasars by cross-matching the optical Quaia [21] and the VLASS catalogs. They found a similar detection rate of ∼4% of their sample.

We found that more than half of the FIRST-detected AGN were detected by VLASS (∼60% of FIRST-detected NL1 AGN and ∼73% of FIRST-detected BL1 AGN). Using from these samples only those galaxies where optical spectral data do not indicate significant optical obscuration, we found that ∼63% and ∼45% of the radio-emitting BL1 and NL1 AGN are radio-loud (RL $>$ 10), respectively. This is consistent with previous results of authors who reported a significant dearth of radio-loud narrow-line type 1 quasars (e.g., [5,32]) compared to broad-line type 1 quasars. The radio-loud fractions of the BLQ1 and the optically fainter BLS1 galaxies are similarly ∼(60–64)%. However, the radio-loud fractions of NLQ1 are lower, ∼35% than those of the NLS1 galaxies, ∼47%.

This also means that surprisingly, we find a large fraction of the Seyfert 1 galaxy subpopulations of the BL1 and NL1 AGN to be formally radio-loud as well, even when just focusing on systems that are known not to be very strongly reddened (and also excluding systems at high redshifts, where reddening information is lacking). This result is unexpected at first glance, given that Seyfert galaxies rarely have bright largely extended radio emission/halos, and given that (broad-line) Seyfert galaxies are rarely of blazar type (i.e., with relativistic jets directed at a small angle to the line of sight, thus, experiencing significant relativistic beaming); blazars are mostly found in quasars. Both bright large-scale radio emission or beaming could have contributed in enhancing their radio emission into the radio-loud regime. We now discuss other scenarios that could enhance the radio emission of Seyfert galaxies into the radio-loud regime.

First, the original sample of [12] is based on optical selection, including also the very faint optical populations, while the radio counterparts were selected using the FIRST with a survey threshold of ∼1 mJy [33], and the cross-matched sample was further constrained by selecting objects detected also in the higher-frequency VLASS observations. Thus, the radio selection is biased towards the relatively compact and radio-bright populations.

Second, the RL can be artificially enhanced by the inclusion of sources experiencing significant host extinction. We tried to mitigate this effect by including only objects with flux density ratios of their Hα and Hβ not exceeding 5. Nevertheless, these objects can still suffer from host extinction; ideally, the limiting ratio should have been set to 3. We also explored this possibility; however, such a cut severely reduced the sample sizes, e.g., only three NLQ1 sources remained, with one of them being radio-loud. Additionally, the results remained the same with optically fainter objects, the Seyfert 1 galaxy subgroups being more radio-loud in both samples. Furthermore, in general, type 1 AGN are not expected to be severely reddened; according to the unified model [34], they are seen near pole-on.

Third, starburst-related radio emission can contribute or even dominate in radio-loud systems. Clear indication of AGN-related radio emission can come from milliarcsecond- (mas-) scale resolution very long baseline interferometry (VLBI) observations. If a compact radio feature with a 1.4-GHz radio power exceeding 2×10^{21} W Hz^{-1} is detected, it must be related to nuclear activity [35]. This means that if a radio source located at $z > 0.1$ is detected with VLBI, its radio emission must come from the AGN since this compact region cannot host enough star-formation-related radio-emitting sources to provide the energy output [36].

Since a VLBI array, due to its narrow field of view, is not a survey instrument, we used the findings of the Deep Extragalactic VLBI–Optical Survey (DEVOS, [37]) to estimate the probable VLBI detection rates. According to DEVOS, ∼85% of FIRST-detected unresolved sources with integrated flux densities > 20 mJy, that have a 'star' type (i.e., unresolved) optical counterpart in SDSS can be detected by VLBI. There are 343 BL1 in the FIRST+VLASS1, 345 BL1 in the FIRST+VLASS2, and 52 NL1 AGN fulfilling these criteria with FIRST compactness values $\gtrsim 0.8$. According to the finding of DEVOS, most of these objects, ∼292 BL1 and ∼42 NL1 sources, are detectable with VLBI technique. Since all but one (a BL1 AGN) are located at redshifts exceeding 0.1, we expect that the radio emission of these objects originate from the central AGN, according to [36]. Thus, as a conservative lower limit (since VLBI non-detection does not exclude the possibility that a radio-emitting AGN can reside in the system), we can hypothesize that at least ∼10% and ∼16% of NL1 and BL1 AGN detected both in the FIRST and VLASS must contain radio-emitting AGN.

Using a different approach, one can compare the SFRs derived from the radio and infrared measurements to assess whether the detected radio emission can be explained solely by star formation or a radio-emitting AGN has to contribute. The high median $\mathrm{SFR_{FIRST}}$ values for all subsamples already show that half of the objects in each subsample have SFRs exceeding $\sim 10^3$ M$_\odot$ yr^{-1} (see Section 3.4). Thus, it is highly probable that at least half of the sources of each subsample must contain a radio-emitting AGN to eliminate the need for unrealistically energetic star formation. Cluver et al. (2017) [38] provide relationships between the infrared luminosities obtained via measurements in the 12 μm (W3) and 24 μm (W4) bands of WISE [39]. They conclude that the tight relation between the W3 luminosity and total infrared luminosity can be used to disentangle star-formation- and AGN-related radio emission.

We cross-matched the FIRST–VLASS samples with the AllWISE catalog [40], and found infrared counterparts with significant detection in the W3 band, with SNR > 3, for 395 and 407 NL1 and 1770 and 1754 BL1 AGN using the first- and second-epoch VLASS data,

respectively. Applying Equation (4) of [38], we calculated the SFR in $M_\odot\ yr^{-1}$ from the W3 luminosities (νL_ν) for these galaxies as

$$\log \mathrm{SFR}_{\mathrm{W3}} = 0.889 \log(\nu L_\nu) - 7.76, \tag{3}$$

where (νL_ν) is in units of $L_\odot$. We used the lower three bands of WISE, 3.4 μm, 4.3 μm, and 12 μm, to estimate the infrared spectral index and used that for the *K*-correction in the luminosity calculation. The obtained SFR values, $\mathrm{SFR}_{\mathrm{W3}}$, are plotted against the SFR obtained from the FIRST data, $\mathrm{SFR}_{\mathrm{FIRST}}$, in Figure 12, where we included only those objects that have radio spectral indices below 2.5 and relative error of radio flux density measurements < 0.3; thus, their FIRST radio power could be reliably calculated. There are 366 and 1670 such NL1 and BL1 AGN, respectively, in FIRST+VLASS1. Since there is no significant difference between FIRST+VLASS1 and FIRST+VLASS2 samples, we only show the results obtained with using the first-epoch VLASS data.

Cluver et al. (2017) [38] provide the relationship between the $\mathrm{SFR}_{\mathrm{W3}}$ and the SFR derived from 1.4-GHz radio observations. This is shown by the black lines in Figure 12. The light green symbols indicate the galaxies most probably containing radio-emitting AGN according to the findings of [37]. All these galaxies are above the line of [38]; thus, two independent methods show these objects most probably contain radio-emitting AGN. Concerning the BL1 and NL1 samples, most of the objects are above the line; nevertheless, the fraction is lower for the NL1 AGN. Specifically, 79% and 91% of the NL1 and BL1 sources are above this relation, respectively, indicating that radio emission from the AGN in these galaxies has to contribute to the observed 1.4-GHz radio power. The fractions of sources where AGN contribute to the radio emission are also larger for the optically brighter quasars than for the fainter Seyfert galaxies, in both the narrow-line and broad-line samples.

We checked the median RL values for those galaxies that, according to the SFR comparison, most likely contain radio-emitting AGN. We found the same result as before, namely, NL1 AGN have lower median RL values (∼17) than BL1 AGN (∼30), and Seyfert 1 galaxies within each sample have larger median RL than type 1 quasars. Thus, it is unlikely that star-formation-related radio emission caused the larger median RL values of Seyfert 1 galaxies.

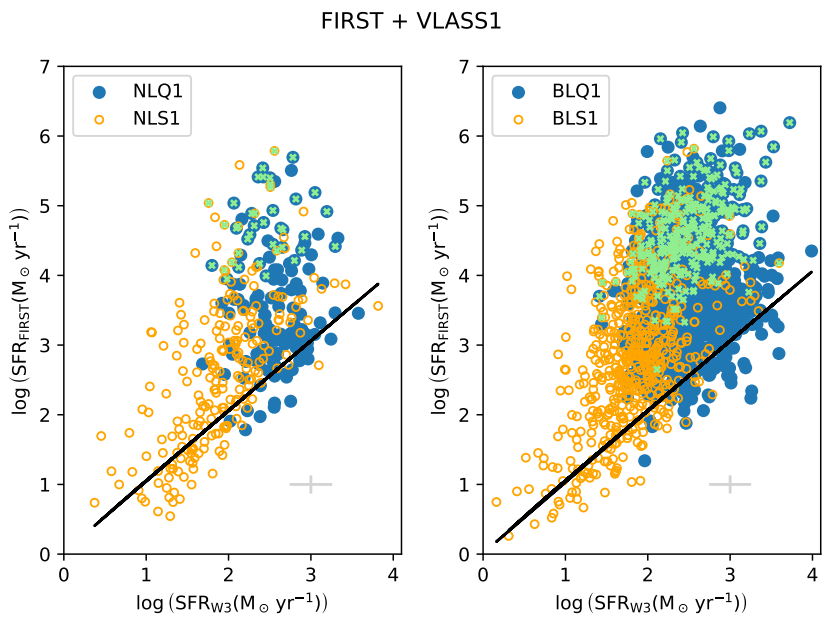

Figure 12. Star formation rates calculated from the 1.4-GHz radio power and from the 12 μm luminosity. Small light green symbols show the galaxies classified as 'star' in SDSS, having a flux

density > 20 mJy in FIRST and a compactness value > 0.8 in FIRST. According to DEVOS [37], these objects have a high probability to be detectable by VLBI. The black solid lines show the relationship between the SFR calculated from the 1.4-GHz radio emission and from the 12 μm luminosity given in [38]. Data points are from the FIRST+VLASS1 sample. Light grey error-bars in the lower right corners illustrate the typical errors of the samples.

4.2. Spectral Index and Radio Variability

Concerning the FIRST–VLASS spectral indices, our median spectral index between 1.4 GHz and 3 GHz obtained for the NL1 sample, −0.49 and −0.45, is in good agreement with the results of [6], −0.61 and −0.47, that were obtained with using the first- and second-epoch VLASS data, respectively. The difference can arise from the fact that we only calculated spectral index for sources that are indicated to have the lowest probability of being observational artifacts in the VLASS catalog and also did not include objects with large relative flux density errors. Varglund et al. (2025) [6] also analyzed 144-MHz LoTSS data [7] and were able to identify a group of NL1 AGN with peaked radio spectra. While we only calculated two-point radio spectral indices, we found that NL1 AGN have different, slightly steeper radio spectra than BL1 AGN, which may indicate difference in their radio-emitting morphology, such as containing slightly more extended features.

While comparing the FIRST and VLASS flux densities, we identified a couple of sources that brightened significantly between their FIRST and VLASS observations. Most of these AGN (one NL1 and four BL1) showed significant variability within ∼3 yr across the three epochs of VLASS observations. However, one NL1 source, SDSS J110546.07+145202.4 (also remarked by [6] as an NLS1 galaxy with unusually large 1.4 GHz–3 GHz radio spectral index) with the most pronounced brightening of a factor of ∼20, showed only hints of variability in the VLASS epochs and seems to remain in an elevated flux density state in the last ∼8 yr [41,42]. Nyland et al. (2020) [43] conducted a somewhat similar study, looking for quasars undetected in FIRST but detected in VLASS with a peak intensity $\gtrsim 3\,\mathrm{mJy\,beam^{-1}}$, thus ensuring a spectral index > 2.5. They found 26 sources transitioned from radio-quiet to radio-loud state within the last ∼20 yr, but they remained at roughly steady flux density levels during the VLASS epochs. According to their follow-up observation, some of the objects have peaked radio spectra, characteristic of young radio AGN [44]. They concluded that they most probably contain compact, young jets.

5. Summary

We investigated the radio properties of a large sample of optically selected NL1 and BL1 active galaxies using the FIRST and VLASS radio catalogs. We separately investigated the first- and second-epoch VLASS data. Our main findings were robust irrespective of which epoch of the VLASS was used.

- We found a 1.4-GHz detection rate of a few percent for both the BL1 and NL1 samples. The detection rate was lower for the narrow-line AGN than for the broad-line ones.
- More than half of the 1.4-GHz-detected NL1 and BL1 AGN were detected at 3 GHz in the VLASS.
- Using the 1.4-GHz FIRST and the 3-GHz VLASS data, we found that on average, NL1 AGN have slightly steeper spectra compared to BL1 AGN, although the median spectral index values obtained are still compatible with flat radio spectra for both samples. According to statistical tests, the spectral index distributions of the NL1 and BL1 AGN are different.
- According to the KS and AD tests, the radio loudness of the NL1 and BL1 samples follow different distributions, with lower median RL values for the NL1 AGN.

- The optically fainter Seyfert 1 galaxies do not have lower median RL value than the optically brighter type 1 quasar samples within either the BL1 or the NL1 samples. We did not see any trend in radio loudness with *B*-band optical absolute magnitude.
- The 1.4-GHz radio power of the NL1 and BL1 AGN detected at both 1.4 and 3-GHz show the expected trend with *B*-band optical absolute magnitude; the radio power increases with increasing optical brightness. The median 1.4-GHz radio power was the largest for the optically brighter BLQ1 and the lowest for the optically fainter NLS1 sample.
- When comparing the SFRs estimated from the radio (FIRST) and infrared (WISE) data, we found that the radio emission of most of the investigated galaxies imply higher SFRs than the infrared emission, indicating that the AGN contribute to the radio emission significantly in those. When comparing the Seyfert 1 galaxies and the type 1 quasars clearly containing radio-emitting AGN, the median RL value of the optically fainter Seyfert 1 galaxies is still higher than that of the type 1 quasars.

In general, NL1 AGN are fainter radio emitters, as shown by both their 1.4-GHz radio power and lower RL values. By selecting AGN detected at both 1.4 GHz and 3 GHz, we mostly picked those objects whose radio emission dominantly originates from an AGN. Thus, the differences seen in the radio emissions mainly arise from the differences in the central engines and not from the existence/lack of star formation in the host galaxies.

Surprisingly, the median RL values of Seyfert 1 galaxies are higher than those of the type 1 quasars in both the narrow- and broad-line samples. However, the 1.4-GHz radio powers are higher for the type 1 quasars and show the expected decreasing trend with decreasing absolute optical magnitude. This apparent discrepancy may arise from the complexity when using the optical brightness derived from the observations of resolved galaxies, which can hinder the accurate estimation of radio loudness.

Our results place the radio comparison of NL1 and BL1 AGN on a more uniform footing by exploiting the large parent catalogs of [12] together with the FIRST and the available catalogs of the first two VLASS epochs. The persistence of the main differences across the two epoch-based analyses shows that these trends are unlikely to be driven by epoch-dependent flux-density variations, even though individual galaxies can display substantial radio variability. In this sense, the lower radio loudness values, lower 1.4-GHz radio power, and the slightly steeper radio spectra found for the NL1 sample most likely reflect genuine population-level differences in their AGN-related radio properties. A natural next step will be to extend this work to a consistently processed multi-epoch framework using the third and fourth epochs of VLASS observations [45], as well as the higher-quality SE data products of the VLASS. The SE catalog is expected to include reliable spectral information within the frequency range of the survey, (2–4) GHz, and would allow the determination of radio spectral index from simultaneous measurements. Thus, a more direct test can be conducted to reveal the roles of radio variability, spectral evolution, and compact radio-source structure in shaping the observed NL1–BL1 differences.

Author Contributions: Conceptualization, K.É.G., S.K. and S.F.; data curation, K.É.G., S.K. and A.M.; methodology, K.É.G. and E.F.-D.; software, K.É.G., A.M. and E.F.-D.; formal analysis, K.É.G. and S.K.; visualization, K.É.G. and E.F.-D.; writing—original draft preparation, K.É.G. and S.K.; writing—review and editing, all authors. All authors have read and agreed to the published version of the manuscript.

Funding: This research was supported by the Hungarian National Research, Development and Innovation Office via the excellence grant TKP2021-NKTA-64 and by HUN-REN Hungarian Research Network.

Data Availability Statement: The NL1 and BL1 data files used in this publication are available at the Zenodo archive at https://doi.org/10.5281/zenodo.20451035 (accessed on 2 June 2026).

Acknowledgments: We thank the anonymous reviewers for providing useful comments that helped to improve our paper. This research has made use of the VizieR catalog access tool, CDS, Strasbourg, France (DOI: 10.26093/cds/vizier). The original description of the VizieR service was published in [46]. We used in our work the Astrogeo VLBI FITS image database, DOI: 10.25966/kyy8-yp57, maintained by Leonid Petrov. This research has made use of the NASA/IPAC Extragalactic Database (NED), which is operated by the Jet Propulsion Laboratory, California Institute of Technology, under contract with the National Aeronautics and Space Administration. Funding for the Sloan Digital Sky Survey IV has been provided by the Alfred P. Sloan Foundation, the U.S. Department of Energy Office of Science, and the Participating Institutions. SDSS-IV acknowledges support and resources from the Center for High Performance Computing at the University of Utah. The SDSS website is www.sdss4.org. SDSS-IV is managed by the Astrophysical Research Consortium for the Participating Institutions of the SDSS Collaboration including the Brazilian Participation Group, the Carnegie Institution for Science, Carnegie Mellon University, Center for Astrophysics | Harvard and Smithsonian, the Chilean Participation Group, the French Participation Group, Instituto de Astrofísica de Canarias, The Johns Hopkins University, Kavli Institute for the Physics and Mathematics of the Universe (IPMU)/University of Tokyo, the Korean Participation Group, Lawrence Berkeley National Laboratory, Leibniz Institut für Astrophysik Potsdam (AIP), Max-Planck-Institut für Astronomie (MPIA Heidelberg), Max-Planck-Institut für Astrophysik (MPA Garching), Max-Planck-Institut für Extraterrestrische Physik (MPE), National Astronomical Observatories of China, New Mexico State University, New York University, University of Notre Dame, Observatário Nacional/MCTI, The Ohio State University, Pennsylvania State University, Shanghai Astronomical Observatory, United Kingdom Participation Group, Universidad Nacional Autónoma de México, University of Arizona, University of Colorado Boulder, University of Oxford, University of Portsmouth, University of Utah, University of Virginia, University of Washington, University of Wisconsin, Vanderbilt University, and Yale University.

Conflicts of Interest: The authors declare no conflicts of interest.

Abbreviations

The following abbreviations are used in this manuscript:

AD	Anderson–Darling
AGN	active galactic nuclei
AIPS	Astronomical Image Processing System
ASKAP	Australian Square Kilometre Array Pathfinder
BADASS	Bayesian AGN Decomposition Analysis for SDSS Spectra
BLR	Broad Line Region
BLS1	Broad-line Seyfert 1
CIRADA	Canadian Initiative for Radio Astronomy Data Analysis
DEVOS	Deep Extragalactic VLBI–Optical Survey
DR	data release
EVN	European VLBI Network
FIRST	Faint Images of the Radio Sky at Twenty-Centimeters
FWHM	full-width at half maximum
IPAC	Infrared Processing and Analysis Center
KS	Kolmogorov–Smirnov
ΛCDM	Lambda Cold Dark Matter
LINER	low-ionization nuclear emission-line region
LOFAR	Low-Frequency Array
LoTSS	Low-Frequency Array Two-metre Sky Survey
MOJAVE	Monitoring of Jets of Active Galactic Nuclei with Very Long Baseline Array Experiments

NASA	National Aeronautics and Space Administration
NLR	Narrow Line Region
NLS1	Narrow-line Seyfert 1
NRAO	National Radio Astronomy Observatory
NVSS	NRAO VLA Sky Survey
RACS	Rapid ASKAP Continuum Survey
RL	radio loudness
SDSS	Sloan Digital Sky Survey
SE	single epoch
SF	star formation
SFR	star formation rate
SNR	signal-to-noise ratio
VLA	Karl G. Jansky Very Large Array
VLASS	VLA Sky Survey
VLBA	Very Long Baseline Array
VLBI	very long baseline interferometry
VSOP	VLBI Space Observatory Program
WISE	Wide-field Infrared Survey Explorer

Appendix A. Optical Galaxies with Multiple Radio Counterparts

We give here the list of NL1 and BL1 AGN with multiple FIRST radio detections (Table A1). In these objects, the FIRST flux densities given in our catalog are the summed flux densities of the FIRST source components. We also indicate whether multiple counterparts are found in the VLASS catalogs. In those cases, the VLASS flux densities in the catalog are the summed flux densities of the counterparts.

Table A1. Objects with multiple FIRST counterparts. The first one is an NL1, the others are all BL1 AGN.

Name	VLASS Counterparts
SDSS J030313.02−001457.5	1
SDSS J003626.98+001303.7	2
SDSS J023814.10−062852.0	2
SDSS J024500.70−074736.4	2
SDSS J083337.36+221244.3	2
SDSS J092307.39+305926.4	2
SDSS J093000.17+250005.7	1
SDSS J105026.03+015138.3	1
SDSS J114707.57+503053.4	2
SDSS J132103.41+123748.2	1
SDSS J134303.59+521626.7	2
SDSS J230545.66−003608.6	1

Appendix B. Statistical Investigations of the Samples' Redshift Distributions

We employed two methods to investigate whether our findings of the spectral index distributions of the different NL1 and BL1 samples (in Section 3.2) are influenced by the different redshift distributions of the samples. In the first approach, we compared the redshift distributions of the samples via the KS and AD statistical tests after applying different redshift cuts, $z_{\rm cut}$. The cut values were chosen between 0.05 and 0.50, in steps of 0.05. For each threshold, we compared the redshift distributions of the NL1–BL1, NLQ1–BLQ1, and NLS1–BLS1 samples separately for the two VLASS epochs. We required both tests to give $p \geq 0.05$ in all six epoch–comparison combinations.

Table A2. Exploratory scan of the redshift-cut used to compare the redshift distributions of the NL1-like and corresponding BL1-like samples. $N_{\rm min}$ is the smallest group size among the six comparisons, comprising the NL1–BL1, NLQ1–BLQ1, and NLS1–BLS1 pairs for FIRST+VLASS1 and FIRST+VLASS2. $\min(p_{\rm KS})$ and $\min(p_{\rm AD})$ are the smallest two-sample KS and AD p-values, respectively, among these six comparisons. $N_{\rm KS}/6$ and $N_{\rm AD}/6$ give the numbers of comparisons for which the corresponding test does not reject the null hypothesis of identical redshift distributions at the adopted significance level of $p = 0.05$. $N_{\rm both}/6$ is the number of comparisons for which neither test rejects the null hypothesis. The first row represents the effectively uncut sample. The bold row at $z_{\rm min} = 0.30$ marks the lowest tested threshold for which neither test rejects the null hypothesis in any of the six comparisons.

$z_{\rm cut}$	$N_{\rm min}$	$\min(p_{\rm KS})$	$\min(p_{\rm AD})$	$N_{\rm KS}/6$	$N_{\rm AD}/6$	$N_{\rm both}/6$
0.00	155	$<10^{-4}$	$\leq$0.001	2/6	2/6	2/6
0.05	155	$<10^{-4}$	$\leq$0.001	2/6	2/6	2/6
0.10	155	0.0001	$\leq$0.001	4/6	4/6	4/6
0.15	154	0.0023	$\leq$0.001	4/6	4/6	4/6
0.20	152	0.0059	0.0046	4/6	4/6	4/6
0.25	151	0.0244	0.0246	4/6	4/6	4/6
0.30	**142**	**0.0643**	**0.0882**	**6/6**	**6/6**	**6/6**
0.35	131	0.0216	0.0157	4/6	4/6	4/6
0.40	114	0.0408	0.0407	5/6	5/6	5/6
0.45	99	0.0733	0.0544	6/6	6/6	6/6
0.50	81	0.1891	0.0673	6/6	6/6	6/6

In Table A2, we list the results of these comparisons. For each $z_{\rm cut}$ value, we give the smallest group size, $N_{\rm min}$, the lowest p-values of the KS and AD tests, $p_{\rm KS}$, $p_{\rm AD}$, respectively, and the number of comparisons, $N_{\rm KS}$, $N_{\rm AD}$ where the KS/AD test failed to reject the null hypothesis (at a significance level of $p = 0.05$) that the redshift of the pairs come from the same redshift distribution. In the last column, we list the number of comparisons for which neither test rejects the null hypothesis. It can be seen that $z_{\rm cut} = 0.3$ was the lowest tested threshold for which neither test rejects the null hypothesis in any of the six comparisons. At this threshold, the minimum KS and AD p-values were 0.0643 and 0.0882, respectively, and the smallest retained group still contained 142 objects. Although the criterion was also satisfied at $z_{\rm cut} = 0.45$ and 0.50, these cuts retained substantially fewer objects, reducing the statistical power of the tests. Therefore, we adopted $z > 0.3$ as the lowest threshold that removed the statistically detectable differences between the redshift distributions without unnecessarily reducing the sample size. The p-values do not necessarily vary monotonically with $z_{\rm cut}$, because each threshold changes both the composition and the size of the retained samples.

Then, we compared the radio spectral index distributions of the whole and the $z > 0.3$ samples. We calculated the median spectral indices and compared the spectral index distributions using the KS and AD tests for the NL1–BL1, NLQ1–BLQ1, and NLS1–BLS1 sample pairs for both VLASS epochs. The null hypothesis was that the two samples are drawn from the same underlying spectral index distributions. The results are given in Table A3.

In the second approach, to control more directly the differences in the redshift distributions, we performed a redshift-matched Monte Carlo resampling analysis for the NL1–BL1, NLQ1–BLQ1, and NLS1–BLS1 comparisons in both VLASS epochs. We divided the samples into redshift bins with a width of $\Delta z = 0.10$. In each redshift bin containing objects from both groups, we randomly selected the same number of sources from the two groups,

$$N_{\rm draw,bin} = \min(N_{\rm NL1-like,bin}, N_{\rm BL1-like,bin}). \quad \text{(A1)}$$

For each realization, we calculated the differences of the median spectral indices, $\Delta\alpha_{\rm zmatch}$, as

$$\Delta\alpha_{\rm zmatch} = {\rm median}(\alpha_{\rm NL1-like}) - {\rm median}(\alpha_{\rm BL1-like}) \quad \text{(A2)}$$

The more negative values of $\Delta\alpha_{\rm zmatch}$ indicate steeper median radio spectra for the NL1-like group. We repeated the procedure 5000 times and characterized the resulting $\Delta\alpha_{\rm zmatch}$ distributions by their median and central 16–84 percentile interval. Unlike the fixed redshift cut, this procedure does not automatically discard all low-redshift sources. It retains the redshift bins in which both groups are represented and directly matches the numbers of objects from the two groups within each bin. It also quantifies the realization-to-realization variation of $\Delta\alpha_{\rm zmatch}$. To test the dependence of the results on the matching parameters, we repeated the analysis using redshift-bin widths of $\Delta z = 0.10$, 0.15, and 0.20, requiring at least 1, 3, or 5 objects from each group in a retained bin. These tests determine whether the conclusions are sensitive to the adopted binning or to sparsely populated redshift bins. We found that the results did not depend on the choice of these parameters.

Table A3. Comparison of the median spectral indices and the results of pairwise comparison of the spectral index distributions with the KS and AD tests for the whole and the $z > 0.3$ samples. The number of sources is given in the third column. The median spectral indices of the two samples are listed in cols. 4 and 5. Here, index 1 and 2 refer to the first and second samples given in column 1. In cols. 6 and 7, the p values of the respective statistical tests are listed. In the last two columns, we report whether the given test rejected the null hypothesis. Results are given for the FIRST+VLASS1 and FIRST+VLASS2 data sets above and below the horizontal line, respectively.

Comparison	Selection	N_1/N_2	Median α_1	Median α_2	$p_{\rm KS}$	$p_{\rm AD}$	KS Reject	AD Reject
NL1–BL1	Full	429/1867	−0.49	−0.32	$<10^{-4}$	$\lesssim$0.001	True	True
	$z > 0.3$	290/1543	−0.49	−0.26	$<10^{-4}$	$\lesssim$0.001	True	True
NLQ1–BLQ1	Full	155/1169	−0.39	−0.26	0.0546	0.0214	False	True
	$z > 0.3$	145/1124	−0.39	−0.23	0.0733	0.0284	False	True
NLS1–BLS1	Full	273/691	−0.56	−0.43	0.0008	$\lesssim$0.001	True	True
	$z < 0.3$	144/416	−0.61	−0.32	0.0001	$\lesssim$0.001	True	True
NL1–BL1	Full	440/1857	−0.45	−0.26	$<10^{-4}$	$\lesssim$0.001	True	True
	$z > 0.3$	297/1540	−0.41	−0.22	$<10^{-4}$	$\lesssim$0.001	True	True
NLQ1–BLQ1	Full	166/1160	−0.32	−0.20	0.0560	0.0081	True	True
	$z > 0.3$	154/1116	−0.31	−0.18	0.0046	0.0105	True	True
NLS1–BLS1	Full	273/692	−0.51	−0.35	0.0003	$\lesssim$0.001	True	True
	$z < 0.3$	142/421	−0.56	−0.29	0.0001	$\lesssim$0.001	True	True

The redshift-matched $\Delta\alpha_{\rm zmatch}$ distributions obtained with the fiducial parameters are shown in Figure A1, and the corresponding numerical results are summarized in Table A4. The redshift-matched median differences remain negative in all six comparisons, and their central 16–84 percentile intervals lie entirely below zero. The matched median differences are less negative than the observed values in all cases, indicating that differences between the redshift distributions may contribute to the measured effect but do not account for it completely. The NL1-like samples retain systematically steeper radio spectra on average after their redshift distributions are directly matched to those of the corresponding BL1-like samples. The ratios of the $\Delta\alpha_{\rm zmatch}$ to $\Delta\alpha_{\rm obs}$ range from 71% to 92%. The ratios are closest to unity for the type 1 quasar subsamples (∼90%), while slightly lower for the Seyfert 1 subsamples (∼80%). Thus, the spectral index difference for the Seyfert 1-like subsamples remains after redshift matching.

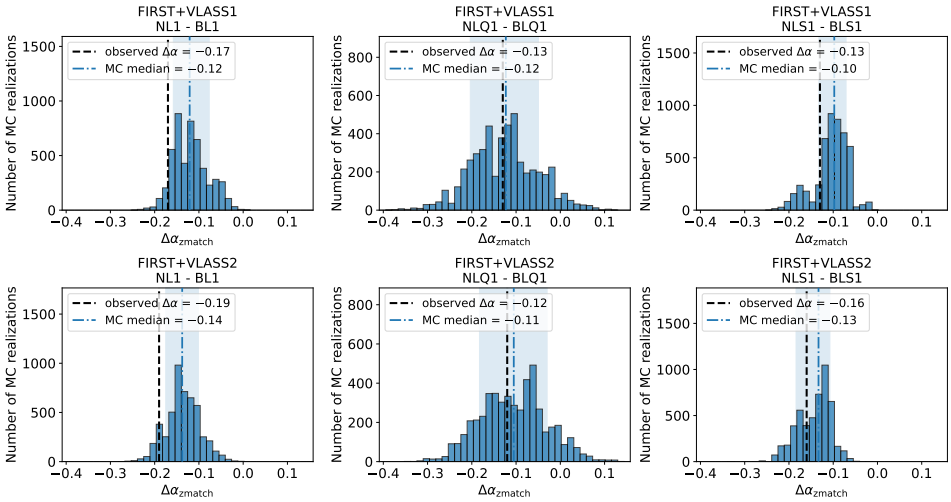

Figure A1. The redshift-matched resampling distributions of the median spectral index differences between the NL1-like and corresponding BL1-like samples. Negative values indicate that the NL1-like group has a steeper median radio spectrum than the corresponding BL1-like group. The upper and lower rows show the FIRST+VLASS1 and FIRST+VLASS2 results, respectively, and from left to right for the full samples, the type 1 quasar-like subsamples, and the Seyfert 1 like subsamples. The black dashed lines mark the observed median differences, while the blue dash-dotted lines show the medians of the redshift-matched distributions. The shaded regions indicate the central 16–84 percentile intervals.

Table A4. The redshift-matched resampling test of the median spectral index differences between the NL1-like and corresponding BL1-like samples. The tested quantity is defined as $\Delta\alpha_{\rm zmatch} = {\rm median}(\alpha_{\rm NL1-like}) - {\rm median}(\alpha_{\rm BL1-like})$, where N_1 and N_2 are the original sample sizes, and $N_{\rm match}$ is the number of matched objects in each group. The quoted intervals correspond to the central 16–84 percentiles of the redshift-matched distributions. Results are given for the FIRST+VLASS1 and FIRST+VLASS2 data sets above and below the horizontal line, respectively.

Comparison	N_1	N_2	$N_{\rm match}$	$\Delta\alpha_{\rm obs}$	$\Delta\alpha_{\rm zmatch,med}$	[16–84%]
NL1–BL1	429	1867	427	−0.17	−0.12	[−0.158, −0.077]
NLQ1–BLQ1	155	1169	153	−0.13	−0.12	[−0.203, −0.049]
NLS1–BLS1	273	691	273	−0.13	−0.10	[−0.132, −0.071]
NL1–BL1	440	1857	438	−0.19	−0.14	[−0.175, −0.101]
NLQ1–BLQ1	166	1160	164	−0.12	−0.11	[−0.183, −0.030]
NLS1–BLS1	273	692	273	−0.16	−0.13	[−0.184, −0.107]

Appendix C. Sources with Large Spectral Indices

The two-point radio spectral index of a few objects exceeded the theoretical value of optically thick synchrotron emission, 2.5. Below, we briefly present the radio properties of these objects and discuss the reasons behind their derived spectral index values.

Appendix C.1. NL1 AGN

In the NL1 sample, SDSS J102818.15+535113.6 and SDSS J110546.07+145202.4 have spectral indices exceeding 2.5. In the case of SDSS J110546.07+145202.4, this is true for both of the VLASS observing epochs, while the 3-GHz flux density of SDSS J102818.15+535113.6 decreased significantly between the two VLASS epochs. Its two-point radio spectral index is 1.4 when the second-epoch VLASS data are used.

SDSS J110546.07+145202.4 is a Seyfert 1 galaxy (located at a redshift of $z = 0.12$) that showed an exceptional brightening by a factor of >20 at centimeter wavelengths during ∼18 yr. Its multi-wavelength radio properties are discussed in detail in [41], and multiple

radio, optical, UV, and X-ray follow-ups and further discussion of outburst scenarios are presented in [42,47].

SDSSJ 102818.15+535113.6 has an absolute B-band optical magnitude of -23.3; thus, it formally can be regarded as a quasar. It is located at a redshift of $z = 0.512$. Its flux density measured at 3 GHz with the VLASS changed significantly over the three epochs: $S^{\mathrm{ep1}} = (12.57 \pm 0.21)$ mJy, $S^{\mathrm{ep2}} = (4.9 \pm 0.25)$ mJy, $S^{\mathrm{ep3}} = (4.8 \pm 0.2)$ mJy. It seems that the source underwent a brightening in 2017 September during the first epoch of the VLASS observations; however, it faded back by 2020 August, when the second epoch of VLASS observations took place. In addition to FIRST, it was also detected in the lower-resolution NRAO VLA Sky Survey, NVSS, [48] with a flux density of (2.5 ± 0.4) mJy. This slightly higher value than the one measured in FIRST, (1.7 ± 0.2) mJy, can be related to resolution issues or variability. We are not aware of more recent 1.4-GHz flux density measurements of the object. At lower frequencies, the source was detected at 150 MHz with the LOFAR within the framework of the LoTSS DR2 [7] with a flux density of $S^{\mathrm{LOFAR}} = (2.5 \pm 0.1)$ mJy.

Appendix C.2. BL1 AGN

Here we present literature details on the eight BL1 AGN that have FIRST–VLASS spectral indices exceeding 2.5. Half of these AGN showed such high spectral index values either using the first- or the second-epoch VLASS data. In one case, SDSSJ111507.65+0237575, the spectral index calculated with the second-epoch VLASS data is 2.3. For two other galaxies, SDSSJ094715.56+631716.4 and SDSSJ130414.70+591623.6, the spectral indices calculated with the first-epoch VLASS data are 2.4, and 2.3, respectively; thus, they formally do not exceed the limiting value of 2.5.

The radio flux density values of the eight BL1 AGN measured in the FIRST, Rapid Australian Square Kilometre Array Pathfinder (ASKAP) Continuum Survey (RACS), and VLASS are given in Table A5. The first-epoch VLASS values are from the third pipeline version VLASS Quick Look catalog. For the second and third epochs, we downloaded the available so-called 'single epoch' (SE) images and the quick-look images, respectively. The SE images are reported to be of higher quality than the quick-look images taken in the same epoch [17]. For SDSS J090007.99+364610.6, a SE image was not available; therefore, we used the flux density value reported in the second pipeline version of the VLASS Quick Look catalog. To obtain the flux densities, we fitted each image with single Gaussian brightness distribution models using the IMFIT task of the National Radio Astronomy Observatory (NRAO) Astronomical Image Processing System (AIPS) [49].

The high spectral indices exceeding 2.5 can be explained with the significant increase in the radio emission that happened between the FIRST and the VLASS observations or, alternatively, a different emission mechanism, i.e., free-free absorption [50]. In the case of six BL1 AGN (Table A5), the comparison of FIRST and the more recent RACS [51] data show the significant brightening at $\sim$1.4 GHz; thus, flux density variability can explain the large spectral indices. Their radio brightenings range from a factor of 2 to 7. Except for SDSS J023932.47+045805.9 and SDSS J111507.65+023757.5, the sources also show significant variability at 3 GHz during the three VLASS epochs.

For two BL1 AGN, we are not aware of more recent 1.4 GHz radio flux density measurements; thus, there is no unambiguous evidence of flux density variability influencing the obtained spectral indices. Nevertheless, the three epochs of VLASS data show the changes of the 3-GHz flux density of these two sources as well.

Table A5. Radio flux densities of BL1 AGN with $\alpha > 2.5$. The spectral index of the objects below the horizontal line exceed 2.5 if the second-epoch VLASS observation is considered. Missing values indicate BL1 AGN not falling into the coverage of the given catalog. For the second-epoch VLASS flux density, we give the value derived from the single-epoch image.

Source Name	FIRST	RACS			VLASS		
	1.4 GHz	0.889 GHz	1.367 GHz	1.655 GHz	3 GHz		
	1994–2009	2019–2020	2020–2022	2021–2022	Sep–Dec 2017	Aug–Oct 2020	Jan–Mar 2023
J001235.72+020326.3	0.8 ± 0.1	8.3 ± 2.6	3.5 ± 0.4	5.1 ± 0.7	7.7 ± 0.3	9.4 ± 0.3	12.7 ± 0.3
J001859.75+061931.9	7.0 ± 0.2	11.3 ± 1.1	29.9 ± 1.8	43.2 ± 4.3	74.3 ± 0.3	70.3 ± 0.3	77.4 ± 0.3
J023932.47+045805.9	0.5 ± 0.1	–	2.0 ± 0.3	2.5 ± 0.4	4.5 ± 0.2	4.9 ± 0.3	5.1 ± 0.3
J090007.99+364610.6 [a]	2.4 ± 0.2	–	16.8 ± 1.3	26.7 ± 2.7	51.6 ± 0.4	63.6 ± 0.2	98.2 ± 0.3
J111507.65+023757.5 [b]	1.6 ± 0.2	1.96 ± 0.5	3.6 ± 0.4	6.4 ± 0.7	12.5 ± 0.2	10.0 ± 0.3	11.0 ± 0.2
J145958.43+333701.7	11.6 ± 0.6	–	65.4 ± 3.9	75.7 ± 8.1	121.5 ± 1.0	90.7 ± 0.2	67.6 ± 0.2
J094715.56+631716.4	2.0 ± 0.2	–	–	–	12.4 ± 0.2	20.2 ± 0.2	18.7 ± 0.2
J130414.70+591623.6	2.0 ± 0.3	–	–	–	11.2 ± 0.2	15.6 ± 0.2 [c]	14.8 ± 0.2

[a] The only galaxy for which a single-epoch VLASS image was not available; therefore, the flux density is obtained from the second-epoch VLASS quick-look catalog. Moreover, the epochs of the VLASS observations of this galaxy are different: May 2019, November 2021, and July 2024. [b] The spectral index of this source is 2.3 if the flux density of the second-epoch VLASS observation is used. [c] The second-epoch VLASS observation took place on 27 June 2020.

The brightest of these galaxies, SDSS J145958.43+333701.7, was studied in detail by [52]. They reported its long-term flux density variability and the results of their VLBI observation of the source. The mas-scale image can be interpreted as SDSS J145958.43+333701.7 being a compact symmetric object or a blazar. Owing to the large apparent speed measured for the radio features, Ref. [52] concluded that the blazar hypothesis is more likely.

Appendix D. The Extremely Radio-Loud AGN

Here, we comment on individual objects that stand out due to their radio loudness, specifically, with $\log(\mathrm{RL}) > 4$. In particular, we also re-evaluate the optical NL1 classification of all systems based on literature data when available and based on re-inspection of the optical SDSS spectra themselves. In large samples, potential misclassifications can occasionally occur; in particular, starburst galaxies or type 2 AGN can potentially be mistaken for NL1 active galaxies. Additionally, we checked VLBI archives to look for potential indications of relativistically beamed jet emission.

Appendix D.1. NL1 AGN with $\log(\mathrm{RL}) > 4$

SDSS J005833.80+062006.0 ($z = 0.593$):

The SDSS host galaxy image and the SDSS spectrum are very red. Broad Hβ and Mg II emission lines are present. Because Hα is redshifted out of the observable band, a reliable extinction estimate is not possible. The red broad-band spectrum clearly points to the presence of significant extinction. For these reasons, we keep this galaxy as a good NL1 candidate in the sample, but it is not included in the RL distribution investigation. We conclude that the radio loudness is overestimated, possibly by a high factor.

Concerning its radio structure, it was detected with VLBI at 8 GHz as a single, mas-scale compact feature in several epochs with a median flux density of ~170 mJy [53].

SDSS J100888.04+073016.6:

This system is also known as 3C 237. Its redshift ($z = 0.068$) given in the SDSS DR16 [26], used by [12], is not the correct redshift. Likely, it arose from a misidentification of the redshifted [O II]3727 Å emission line with Hβ. The correct redshift, which is reported in multiple data bases and that properly matches the Balmer lines and all other emission

lines, is $z = 0.877$. In fact, in the original catalog of 3C radio sources, the larger redshift, $z = 0.877$ is given [54]. This value is further used and confirmed by the spectral-line measurements of [55]. Additionally, the SDSS DR13 online tool[4] gives a very similar redshift value, 0.881, reported within the framework of the Baryon Oscillation Spectroscopic Survey program [56].

There is a detection of the Hα-[N II] complex in the near-infrared spectrum [55]. The whole unresolved complex has a FWHM $= (2000 \pm 500)$ km s^{-1}, still consistent with the idea that we see NLR emission. The strong [O II]3727 Å line and the red host galaxy suggest that we may see a low-ionization nuclear emission-line region (LINER) emission. The Balmer lines appear as broad as forbidden lines, and there is no Fe II recognizable either. In summary, many different criteria all falsify the NL1 classification of this object. Therefore, we removed it from the sample of NL1 AGN.

In the radio regime, 3C 237 shows a $\sim$1.4′-wide separated double-lobed feature at 1.6 GHz in the European VLBI Network (EVN) observation of [57]. They concluded that the radio jets are most probably oriented close to the plane of the sky.

SDSS J140333.35+085944.0 ($z = 0.45$):

The SDSS host galaxy image and the SDSS spectrum are very red. Strong forbidden transitions are present, the [O II]3727 Å line is significantly stronger than the [O III]5007 Å one, and the Balmer lines are faint in comparison to the forbidden lines. This galaxy is most likely classified as a heavily reddened Seyfert type 1.9 with a strong starburst component. Because of the heavy reddening, the radio loudness of this system cannot be determined, and we do not find positive evidence for its NLS1 classification. Therefore, we did not include this system in our analysis of NL1 galaxies.

Concerning its radio properties, it was observed with the Very Long Baseline Array (VLBA) at 5 GHz in 2015 as a single compact feature with $\sim$10 mJy flux density. It is included in the Radio Fundamental Catalog [53].

SDSS J161432.25+394444.8 ($z = 0.891$):

The broad-band SDSS spectrum of this galaxy is flat, missing any rise towards the blue. A broad component in the Hβ line is present, as well as a highly broadened Mg II emission line. Given the high redshift, the spectrum is relatively noisy, and a visual confirmation of the presence of Fe II emission complexes is not possible. Because Hα is redshifted out of the observable band, a reliable extinction estimate is not possible, even though the absence of a big blue bump is consistent with excess extinction. For these reasons, we keep this galaxy as an NL1 candidate in the sample, but it is not included in the RL distribution investigation. We caution that the radio loudness is likely strongly overestimated.

This object was among the DEVOS targets observed with the EVN at 5 GHz [37]. It was only marginally detected with $\sim$1 mJy flux density, at a significant offset ($\sim$0.7″) from the SDSS optical position. The EVN data indicate that the radio source is almost fully resolved on mas scale.

SDSS J225221.75−004229.5 ($z = 0.77$):

This is another very red galaxy. There may be a faint broad Balmer component present in the spectrum and broad Mg II emission line, but no Fe II is recognizable. The spectrum is more consistent with a heavily obscured intermediate-type Seyfert galaxy than an NLS1 galaxy. Therefore, we removed this system from our NL1 sample. Concerning its radio properties, it was detected as a single mas-scale compact feature of 40 mJy at 8 GHz in a VLBA observation in 2020 [53].

Appendix D.2. BL1 AGN with $\log(\mathrm{RL}) > 4$

SDSS J012156.85+042224.8 ($z = 0.637$):

The SDSS spectrum shows a bona-fide type 1 AGN with strong broad and narrow emission lines. The Hβ profile indicates a type 1.5 AGN. Because the Hα line is redshifted out of the observable band, a reliable extinction estimate is not possible. Since the broad-band spectrum is slightly blue, we keep this galaxy as a BL1 in the sample. We caution that the radio loudness value might be overestimated.

SDSS J012156.85+042224.8 is monitored at 15 GHz within the framework of the Monitoring of Jets of Active Galactic Nuclei with Very Long Baseline Array Experiments (MOJAVE) program [58] and shows a one-sided core–jet structure. It was also detected with the VLBI Space Observatory Program (VSOP) at 5 GHz, with a core brightness temperature of $\sim 9 \times 10^{11}$ K [59]. Compared to the equipartition limit of intrinsic brightness temperature, $\sim 5 \times 10^{10}$ K [60], the measured value implies relativistic beaming, the object is a blazar, and its jet is seen at small angle to the line of sight.

SDSS J012141.59+114950.4 ($z = 0.57$):

The SDSS spectrum slightly rises towards the blue and shows evidence for faint broad Hβ emission, indicating a type 1.8 AGN and strong broad Mg II emission line. Hα is just at the edge of the observable band so that an extinction estimate is not possible. This type 1 AGN spectrum may be reddened, and we caution that the radio loudness may be overestimated.

SDSS J012141.59+114950.4 is also part of the MOJAVE sample [58]. Its jet components show apparent superluminal motion with a speed of $\sim$19c (where c denotes the speed of light), indicating a relativistically beamed jet emission observed at small angle to the line of sight [61]. Thus, this source is also a blazar.

SDSS J074125.73+270645.3 ($z = 0.772$):

The SDSS image shows a blue host galaxy, and the SDSS spectrum is blue, with a strong broad Hβ and Mg II emission lines, implying a bona-fide type 1 AGN. Even though the Hα line is redshifted out of the observable band and is not available for an extinction estimate, this AGN does not appear to be heavily reddened and the radio loudness estimate is therefore reliable.

According to 5- and 8-GHz VLBI observations of [62], this object shows a flat-spectrum core and two-sided, steep-spectrum jet structure at mas-scale resolution. It is classified as a compact symmetric object [44]; thus, its radio emission is not dominated by relativistic beaming.

SDSS J080413.87+470442.8 ($z = 0.51$):

This object is also known as 4C 47.27. The SDSS image shows a red host galaxy, and the SDSS spectrum is flat. It is dominated by strong [O III] line emission; a faint broad component of Hβ is recognizable, as well as strong broad Mg II emission. The Hα line is unobservable. This type 1 AGN spectrum may be reddened, and we caution that the radio loudness may be overestimated.

According to the 8-GHz VLBI observation of [63], the mas-scale radio emission originates from a region of $\sim 1''$ containing a bent jet and a faint core.

Notes

1 https://cirada.ca/vlasscatalogueql0 (accessed on 2 June 2026).

2 Version: 26 July 2023, https://ws.cadc-ccda.hia-iha.nrc-cnrc.gc.ca/files/vault/cirada/tutorials/CIRADA__VLASS_catalogue_documentation_2023_june.pdf (accessed on 10 January 2025).

[3] https://ned.ipac.caltech.edu/extinction_calculator (accessed on 2 June 2026) and the script of M. Mechtley https://github.com/mmechtley/ned_extinction_calc (accessed on 2 June 2026).
[4] https://skyserver.sdss.org/dr13/en/tools/explore/summary.aspx (accessed on 2 June 2026).

References

1. Osterbrock, D.E.; Pogge, R.W. The spectra of narrow-line Seyfert 1 galaxies. *Astrophys. J.* **1985**, *297*, 166–176. [CrossRef] [PubMed]
2. Goodrich, R.W. Spectropolarimetry of "Narrow-Line" Seyfert 1 Galaxies. *Astrophys. J.* **1989**, *342*, 224. [CrossRef] [PubMed]
3. Véron-Cetty, M.P.; Joly, M.; Véron, P. The unusual emission line spectrum of I Zw 1. *Astron. Astrophys.* **2004**, *417*, 515–525. [CrossRef]
4. Komossa, S. Narrow-line Seyfert 1 Galaxies. *Rev. Mex. Astron. Astrofis. Conf. Ser.* **2008**, *32*, 86–92. [CrossRef]
5. Komossa, S.; Voges, W.; Xu, D.; Mathur, S.; Adorf, H.M.; Lemson, G.; Duschl, W.J.; Grupe, D. Radio-loud Narrow-Line Type 1 Quasars. *Astron. J.* **2006**, *132*, 531–545. [CrossRef]
6. Varglund, I.; Järvelä, E.; Hardcastle, M.J.; Varglund, S.; Lähteenmäki, A. A comprehensive radio study of narrow-line Seyfert 1 galaxies. *Astron. Astrophys.* **2025**, *703*, A202. [CrossRef]
7. Shimwell, T.W.; Hardcastle, M.J.; Tasse, C.; Best, P.N.; Röttgering, H.J.A.; Williams, W.L.; Botteon, A.; Drabent, A.; Mechev, A.; Shulevski, A.; et al. The LOFAR Two-metre Sky Survey. V. Second data release. *Astron. Astrophys.* **2022**, *659*, A1. [CrossRef]
8. Yuan, W.; Zhou, H.Y.; Komossa, S.; Dong, X.B.; Wang, T.G.; Lu, H.L.; Bai, J.M. A Population of Radio-Loud Narrow-Line Seyfert 1 Galaxies with Blazar-Like Properties? *Astrophys. J.* **2008**, *685*, 801–827. [CrossRef] [PubMed]
9. Foschini, L.; Lister, M.L.; Andernach, H.; Ciroi, S.; Marziani, P.; Antón, S.; Berton, M.; Dalla Bontà, E.; Järvelä, E.; Marchã, M.J.M.; et al. A New Sample of Gamma-Ray Emitting Jetted Active Galactic Nuclei. *Universe* **2022**, *8*, 587. [CrossRef]
10. Gabányi, K.É.; Frey, S.; Perger, K.; Kun, E. Solid Identification of Extragalactic Gamma-Ray Source Using High-Resolution Radio Interferometric Observation. *Universe* **2025**, *11*, 83. [CrossRef]
11. Marziani, P.; del Olmo, A.; D'Onofrio, M.; Dultzin, D.; Negrete, C.A.; Martínez-Aldama, M.L.; Bon, E.; Bon, N.; Stirpe, G.M. Narrow-line Seyfert 1s: What is wrong in a name? In Proceedings of the Revisiting Narrow-Line Seyfert 1 Galaxies and Their Place in the Universe, Padua, Italy, 9–13 April 2018; p. 2. [CrossRef]
12. Paliya, V.S.; Stalin, C.S.; Domínguez, A.; Saikia, D.J. Narrow-line Seyfert 1 galaxies in Sloan Digital Sky Survey: A new optical spectroscopic catalogue. *Mon. Not. R. Astron. Soc.* **2024**, *527*, 7055–7069. [CrossRef]
13. Abdurro'uf; Accetta, K.; Aerts, C.; Silva Aguirre, V.; Ahumada, R.; Ajgaonkar, N.; Filiz Ak, N.; Alam, S.; Allende Prieto, C.; Almeida, A.; et al. The Seventeenth Data Release of the Sloan Digital Sky Surveys: Complete Release of MaNGA, MaStar, and APOGEE-2 Data. *Astrophys. J. Suppl. Ser.* **2022**, *259*, 35. [CrossRef]
14. Wu, Q.; Shen, Y. A Catalog of Quasar Properties from Sloan Digital Sky Survey Data Release 16. *Astrophys. J. Suppl. Ser.* **2022**, *263*, 42. [CrossRef]
15. Sexton, R.O.; Matzko, W.; Darden, N.; Canalizo, G.; Gorjian, V. Bayesian AGN Decomposition Analysis for SDSS spectra: A correlation analysis of [O III] λ5007 outflow kinematics with AGN and host galaxy properties. *Mon. Not. R. Astron. Soc.* **2021**, *500*, 2871–2895. [CrossRef]
16. White, R.L.; Becker, R.H.; Helfand, D.J.; Gregg, M.D. A Catalog of 1.4 GHz Radio Sources from the FIRST Survey. *Astrophys. J.* **1997**, *475*, 479–493. [CrossRef] [PubMed]
17. Lacy, M.; Baum, S.A.; Chandler, C.J.; Chatterjee, S.; Clarke, T.E.; Deustua, S.; English, J.; Farnes, J.; Gaensler, B.M.; Gugliucci, N.; et al. The Karl G. Jansky Very Large Array Sky Survey (VLASS). Science Case and Survey Design. *Publ. Astron. Soc. Pac.* **2020**, *132*, 035001. [CrossRef]
18. Schmidt, M.; Green, R.F. Quasar evolution derived from the Palomar bright quasar survey and other complete quasar surveys. *Astrophys. J.* **1983**, *269*, 352–374. [CrossRef]
19. Arsenov, N.; Frey, S.; Kovács, A.; Slavcheva-Mihova, L. Radio-loudness Statistics of Quasars from Quaia-VLASS. *Astrophys. J. Suppl. Ser.* **2025**, *280*, 23. [CrossRef]
20. Orosz, G.; Frey, S. Optical-radio positional offsets for active galactic nuclei. *Astron. Astrophys.* **2013**, *553*, A13. [CrossRef]
21. Storey-Fisher, K.; Hogg, D.W.; Rix, H.W.; Eilers, A.C.; Fabbian, G.; Blanton, M.R.; Alonso, D. Quaia, the Gaia-unWISE Quasar Catalog: An All-sky Spectroscopic Quasar Sample. *Astrophys. J.* **2024**, *964*, 69. [CrossRef]
22. Abebe, T.H. The Derivation and Choice of Appropriate Test Statistic (Z, t, F and Chi-Square Test) in Research Methodology. *Math. Lett.* **2020**, *5*, 33–40. [CrossRef]
23. Blum, J.R.; Kiefer, J.; Rosenblatt, M. Distribution Free Tests of Independence Based on the Sample Distribution Function. *Ann. Math. Stat.* **1961**, *32*, 485–498. [CrossRef]
24. Anderson, T.W.; Darling, D.A. A Test of Goodness of Fit. *J. Am. Stat. Assoc.* **1954**, *49*, 765–769. [CrossRef]
25. Kellermann, K.I.; Sramek, R.; Schmidt, M.; Shaffer, D.B.; Green, R. VLA Observations of Objects in the Palomar Bright Quasar Survey. *Astron. J.* **1989**, *98*, 1195. [CrossRef] [PubMed]

26. Ahumada, R.; Allende Prieto, C.; Almeida, A.; Anders, F.; Anderson, S.F.; Andrews, B.H.; Anguiano, B.; Arcodia, R.; Armengaud, E.; Aubert, M.; et al. The 16th Data Release of the Sloan Digital Sky Surveys: First Release from the APOGEE-2 Southern Survey and Full Release of eBOSS Spectra. *Astrophys. J. Suppl. Ser.* **2020**, *249*, 3. [CrossRef]
27. Bessell, M.S. UBVRI photometry II: The Cousins VRI system, its temperature and absolute flux calibration, and relevance for two-dimensional photometry. *Publ. Astron. Soc. Pac.* **1979**, *91*, 589–607. [CrossRef]
28. Dong, X.B.; Zhou, H.Y.; Wang, T.G.; Wang, J.X.; Li, C.; Zhou, Y.Y. Partially Obscured Quasars in the Sloan Digital Sky Survey Early Data Release. *Astrophys. J.* **2005**, *620*, 629–645. [CrossRef]
29. Dong, X.; Wang, T.; Wang, J.; Yuan, W.; Zhou, H.; Dai, H.; Zhang, K. Broad-line Balmer decrements in blue active galactic nuclei. *Mon. Not. R. Astron. Soc.* **2008**, *383*, 581–592. [CrossRef]
30. Kharb, P.; Subramanian, S.; Das, M.; Vaddi, S.; Paragi, Z. The Nature of Jets in Double-peaked Emission-line AGN in the KISSR Sample. *Astrophys. J.* **2021**, *919*, 108. [CrossRef]
31. Hopkins, A.M.; Miller, C.J.; Nichol, R.C.; Connolly, A.J.; Bernardi, M.; Gómez, P.L.; Goto, T.; Tremonti, C.A.; Brinkmann, J.; Ivezić, Ž.; et al. Star Formation Rate Indicators in the Sloan Digital Sky Survey. *Astrophys. J.* **2003**, *599*, 971–991. [CrossRef] [PubMed]
32. Rakshit, S.; Stalin, C.S.; Chand, H.; Zhang, X.G. A Catalog of Narrow Line Seyfert 1 Galaxies from the Sloan Digital Sky Survey Data Release 12. *Astrophys. J. Suppl. Ser.* **2017**, *229*, 39. [CrossRef]
33. Helfand, D.J.; White, R.L.; Becker, R.H. The Last of FIRST: The Final Catalog and Source Identifications. *Astrophys. J.* **2015**, *801*, 26. [CrossRef]
34. Antonucci, R. Unified models for active galactic nuclei and quasars. *Annu. Rev. Astron. Astrophys.* **1993**, *31*, 473–521. [CrossRef]
35. Kewley, L.J.; Heisler, C.A.; Dopita, M.A.; Sutherland, R.; Norris, R.P.; Reynolds, J.; Lumsden, S. Compact Radio Emission from Warm Infrared Galaxies. *Astrophys. J.* **2000**, *530*, 704–718. [CrossRef] [PubMed]
36. Middelberg, E.; Deller, A.; Morgan, J.; Rottmann, H.; Alef, W.; Tingay, S.; Norris, R.; Bach, U.; Brisken, W.; Lenc, E. Wide-field VLBA observations of the Chandra deep field South. *Astron. Astrophys.* **2011**, *526*, A74. [CrossRef]
37. Frey, S.; Gurvits, L.I.; Paragi, Z.; Mosoni, L.; Garrett, M.A.; Garrington, S.T. Deep extragalactic VLBI-optical survey (DEVOS). II. Efficient VLBI detection of SDSS quasars. *Astron. Astrophys.* **2008**, *477*, 781–787. [CrossRef]
38. Cluver, M.E.; Jarrett, T.H.; Dale, D.A.; Smith, J.D.T.; August, T.; Brown, M.J.I. Calibrating Star Formation in WISE Using Total Infrared Luminosity. *Astrophys. J.* **2017**, *850*, 68. [CrossRef]
39. Wright, E.L.; Eisenhardt, P.R.M.; Mainzer, A.K.; Ressler, M.E.; Cutri, R.M.; Jarrett, T.; Kirkpatrick, J.D.; Padgett, D.; McMillan, R.S.; Skrutskie, M.; et al. The Wide-field Infrared Survey Explorer (WISE): Mission Description and Initial On-orbit Performance. *Astron. J.* **2010**, *140*, 1868–1881. [CrossRef]
40. Cutri, R.M.; Wright, E.L.; Conrow, T.; Fowler, J.W.; Eisenhardt, P.R.M.; Grillmair, C.; Kirkpatrick, J.D.; Masci, F.; McCallon, H.L.; Wheelock, S.L.; et al. *VizieR Online Data Catalog: AllWISE Data Release (Cutri+ 2013)*; IPAC/Caltech: Pasadena, CA, USA, 2021.
41. Gabányi, K.É.; Komossa, S.; Kraus, A.; Mezősi, A.; Frey, S. Discovery of a giant radio outburst of the narrow-line Seyfert 1 galaxy SDSS J110546.07+145202.4. *Astron. Astrophys.* **2025**, *702*, L17. [CrossRef]
42. Komossa, S.; Grupe, D.; Kraus, A.; Edwards, P.G.; Kerrison, E.F.; Rose, K.; Soria, R.; An, T.; Hardcastle, M.J.; Gabányi, K.É.; et al. SDSS J110546.07+145202.4: The First Long-duration Radio Changing-look NLS1 Galaxy. *Astrophys. J.* **2026**, *1003*, 46. [CrossRef]
43. Nyland, K.; Dong, D.Z.; Patil, P.; Lacy, M.; van Velzen, S.; Kimball, A.E.; Sarbadhicary, S.K.; Hallinan, G.; Baldassare, V.; Clarke, T.E.; et al. Quasars That Have Transitioned from Radio-quiet to Radio-loud on Decadal Timescales Revealed by VLASS and FIRST. *Astrophys. J.* **2020**, *905*, 74. [CrossRef]
44. O'Dea, C.P.; Saikia, D.J. Compact steep-spectrum and peaked-spectrum radio sources. *Astron. Astrophys. Rev.* **2021**, *29*, 3. [CrossRef]
45. Myers, S.T. The VLA Sky Survey (VLASS) and Beyond: Lessons, Challenges, and Future Surveys. In Proceedings of the 2025 United States National Committee of URSI National Radio Science Meeting (USNC-URSI NRSM), Boulder, CO, USA, 7–10 January 2025; p. 226. [CrossRef]
46. Ochsenbein, F.; Bauer, P.; Marcout, J. The VizieR database of astronomical catalogues. *Astron. Astrophys. Suppl.* **2000**, *143*, 23–32. [CrossRef]
47. Dou, L.; Chen, Z.; Wu, J.; Jiang, N.; Shu, X.; Wang, T.; Li, X.; Wang, G.; Ai, Y.; Chen, M.; et al. A Radio Changing-state Jet in the Narrow-line Seyfert 1 Galaxy J1105+1452. *Astrophys. J. Lett.* **2026**, *1002*, L16. [CrossRef]
48. Condon, J.J.; Cotton, W.D.; Greisen, E.W.; Yin, Q.F.; Perley, R.A.; Taylor, G.B.; Broderick, J.J. The NRAO VLA Sky Survey. *Astron. J.* **1998**, *115*, 1693–1716. [CrossRef] [PubMed]
49. Greisen, E.W. AIPS, the VLA, and the VLBA. In *Proceedings of the Information Handling in Astronomy—Historical Vistas*; Heck, A., Ed.; Astrophysics and Space Science Library; Springer: Berlin/Heidelberg, Germany, 2003; Volume 285, p. 109. [CrossRef]
50. Rodriguez, L.F.; Marti, J.; Canto, J.; Moran, J.M.; Curiel, S. Possible radio spectral indices from inhomogeneous free-free sources. *Rev. Mex. Astron. Astrofis.* **1993**, *25*, 23–29.
51. McConnell, D.; Hale, C.L.; Lenc, E.; Banfield, J.K.; Heald, G.; Hotan, A.W.; Leung, J.K.; Moss, V.A.; Murphy, T.; O'Brien, A.; et al. The Rapid ASKAP Continuum Survey I: Design and first results. *Publ. Astron. Soc. Aust.* **2020**, *37*, e048. [CrossRef]

52. Orienti, M.; Dallacasa, D. Variability and parsec-scale radio structure of candidate compact symmetric objects. *Mon. Not. R. Astron. Soc.* **2020**, *499*, 1340–1355. [CrossRef]
53. Petrov, L.Y.; Kovalev, Y.Y. The Radio Fundamental Catalog. I. Astrometry. *Astrophys. J. Suppl. Ser.* **2025**, *276*, 38. [CrossRef]
54. Spinrad, H.; Djorgovski, S.; Marr, J.; Aguilar, L. A third update of the status of the 3 CR sources: Further new redshifts and new identifications of distant galaxies. *Publ. Astron. Soc. Pac.* **1985**, *97*, 932–961. [CrossRef] [PubMed]
55. Hirst, P.; Jackson, N.; Rawlings, S. Near-infrared spectroscopy of powerful compact steep-spectrum radio sources. *Mon. Not. R. Astron. Soc.* **2003**, *346*, 1009–1020. [CrossRef]
56. Dawson, K.S.; Kneib, J.P.; Percival, W.J.; Alam, S.; Albareti, F.D.; Anderson, S.F.; Armengaud, E.; Aubourg, É.; Bailey, S.; Bautista, J.E.; et al. The SDSS-IV Extended Baryon Oscillation Spectroscopic Survey: Overview and Early Data. *Astron. J.* **2016**, *151*, 44. [CrossRef]
57. Fanti, C.; Fanti, R.; Parma, P.; Schilizzi, R.T.; van Breugel, W.J.M. Compact steep spectrum 3 CR radio sources. VLBI observations at 18 cm. *Astron. Astrophys.* **1985**, *143*, 292–306.
58. Lister, M.L.; Aller, M.F.; Aller, H.D.; Hodge, M.A.; Homan, D.C.; Kovalev, Y.Y.; Pushkarev, A.B.; Savolainen, T. MOJAVE. XV. VLBA 15 GHz Total Intensity and Polarization Maps of 437 Parsec-scale AGN Jets from 1996 to 2017. *Astrophys. J. Suppl. Ser.* **2018**, *234*, 12. [CrossRef]
59. Dodson, R.; Fomalont, E.B.; Wiik, K.; Horiuchi, S.; Hirabayashi, H.; Edwards, P.G.; Murata, Y.; Asaki, Y.; Moellenbrock, G.A.; Scott, W.K.; et al. The VSOP 5 GHz Active Galactic Nucleus Survey. V. Imaging Results for the Remaining 140 Sources. *Astrophys. J. Suppl. Ser.* **2008**, *175*, 314–355. [CrossRef] [PubMed]
60. Readhead, A.C.S. Equipartition Brightness Temperature and the Inverse Compton Catastrophe. *Astrophys. J.* **1994**, *426*, 51. [CrossRef] [PubMed]
61. Lister, M.L.; Homan, D.C.; Hovatta, T.; Kellermann, K.I.; Kiehlmann, S.; Kovalev, Y.Y.; Max-Moerbeck, W.; Pushkarev, A.B.; Readhead, A.C.S.; Ros, E.; et al. MOJAVE. XVII. Jet Kinematics and Parent Population Properties of Relativistically Beamed Radio-loud Blazars. *Astrophys. J.* **2019**, *874*, 43. [CrossRef]
62. Tremblay, S.E.; Taylor, G.B.; Ortiz, A.A.; Tremblay, C.D.; Helmboldt, J.F.; Romani, R.W. Compact symmetric objects and supermassive binary black holes in the VLBA Imaging and Polarimetry Survey. *Mon. Not. R. Astron. Soc.* **2016**, *459*, 820–840. [CrossRef]
63. Dallacasa, D.; Tinti, S.; Fanti, C.; Fanti, R.; Gregorini, L.; Stanghellini, C.; Vigotti, M. The B3-VLA CSS sample. II. VLBA images at 18 cm. *Astron. Astrophys.* **2002**, *389*, 115–125. [CrossRef]

Disclaimer/Publisher's Note: The statements, opinions and data contained in all publications are solely those of the individual author(s) and contributor(s) and not of MDPI and/or the editor(s). MDPI and/or the editor(s) disclaim responsibility for any injury to people or property resulting from any ideas, methods, instructions or products referred to in the content.